Formation and modification of wrinkle ridges in the central Tharsis region of Mars as constrained by detailed geomorphological mapping and landform analysis

An Yin[1] and Yingchi Wang[1]

[1]Department of Earth, Planetary, and Space Sciences, University of California

December 13, 2022

Formation and modification of wrinkle ridges in the central Tharsis region of Mars as constrained by detailed geomorphological mapping and landform analysis

An Yin (ayin54@gmail.com) and Yingchi Wang, Department of Earth, Planetary, and Space Sciences, University of California, Los Angeles, CA 90095-1567, USA

Submitted to: Earth and Planetary Physics

Date of Submission: December 11, 2022

Abstract

Wrinkle ridges are common landforms documented on all rocky planets and the Moon in the inner solar system. Despite the long research history, their formation mechanisms remain debated. A key unresolved issue is whether the wrinkle-ridge formation is related to igneous processes. This is because wrinkle ridges are mostly associated in space and possible with time to the occurrence of flood-basalt volcanism in all cases on the rocky bodies in the inner solar system. To address this issue, we conducted geomorphological mapping, topographic-data analysis, and detailed landform analysis of satellite images at the resolution of 25 cm/pixel to 6 m/pixel in the central Tharsis region of Mars. The main result of this work is in the form of (1) a regional geomorphological map at the resolution 6 m/pixel and (2) a local geomorphological map at the resolution of 50 cm/pixel. Our work suggests the following sequence of events in the study area: (1) the creation of a plateau region along the eastern margin of the Tharsis rise by horizontal shortening, (2) the coeval formation of a western volcanic plateau as the source of east-flowing lavas terminating in the east against the tectonically generated eastern plateau, (3) wrinkle-ridge formation by folding in recently emplaced warm and ductile volcanic-lava piles, (4) emplacement of an ice sheet over the Tharsis region that produced extensive boulder-bearing materials, striated surfaces, and boulder-bearing dendritic ridge networks possibly representing glacial eskers, and (5) deposition of locally highly concentrated glacial flours during deglaciation that resulted in the formation of mantled terrain. Our work supports the early suggestion that the Tharsis wrinkle ridges were created by horizontal shortening induced by crustal-scale tectonic processes. In detail, however, the occurrence of flow-front-like margins of many mapped wrinkle ridges suggests ductile folding, which we attribute to the thermally weakened lava piles emplaced during or immediately before the folding event. Post-folding glacial modification means that the present

wrinkle-ridge morphologies may differ significantly from the true fold shapes, which prevent their utilities for inverting subsurface thrust geometries.

1. Introduction

Wrinkle ridges are linear or sinuous arch-shaped topographic features that may be superposed locally by smaller crenulated ridges (e.g., Watters, 1988; Andrews-Hanna, 2020). Wrinkle ridges, originally referred to as “mountain ridges” on flat mare plains of the Moon by T. Gywn Elger (p. 12, 1895) and assigned as a subclass of “elementary rings” by Fielder (1965) and Guest and Fielder (1968), are classified as a distinctive class of landforms on the Moon (Fielder, 1961; Fielder and Kiang, 1962; Fielder, 1965). Subsequent work on lunar wrinkle ridges has quantified their map-view patterns, cross-sectional shapes, spatial distributions, geologic contexts, and formation ages (e.g., Tjia, 1970; Strom, 1972; Bryan, 1973; Plescia and Golombek, 1986; Watters, 1988; Yue et al., 2015, 2019; Li et al., 2018; Watters, 2022). Images collected by spacecrafts through the inner solar system show that linear and sinuous positive landforms similar to lunar wrinkle ridges occur on all rocky planets in the inner solar system: (1) Mercury (Murray et al., 1974; Strom et al., 1975; Strom, 1979; Maxwell and Gifford, 1980; Murchie et al., 2008; Watters et al., 2009a, 2009b; Byrne et al., 2014; Schleicher et al., 2019; Crane and Klimczak, 2019; Watters, 2021), (2) Venus (Watters, 1992; McGill, 1993; Kreslavsky and Basilevsky, 1998; Bilotti and Suppe, 1999; McGill, 2004; Basilevsky and Head, 2006; Ivanov and Head, 2011; Byrne et al., 2021), (3) Mars (Wilhelms, 1974; Carr et al., 1977; Lucchitta, 1978; Greeley and Spudis, 1978a; Greeley and Spudis, 1978b; Lucchitta and Klockenbrink, 1981, Watters, 1991, 1993; Watters and Robinson, 1997; Mangold et al., 1998; Schultz, 2000; Golombek et al., 2001; Head et al., 2002; Montési and Zuber, 2003; Mueller and Golombek, 2004; Ruj and Kawai, 2021; Karagoz et al., 2022a, 2022b), and (4) the Earth (Plescia and Golombek, 1986). A shared characteristic of wrinkle ridges in the inner solar system is that they are closely associated in space and possibly in time to flood-basalt volcanism (e.g., Plescia and Golombek, 1986; Watters, 1988).

Wrinkle-ridge formation has been attributed to horizontal shortening, and the required compressive stresses are thought to have originated from (1) flexural bending of lithosphere caused by lava-fill-induced loading (e.g., Baldwin, 1968; Maxwell et al., 1975) or (2) sinking of high-density bodies in the viscous mantle that causes downward warping of the crust (Phillips et al., 1972; Solomon and Head, 1979, 1980; Freed et al., 2001). Tjia (1970) notes that some lunar wrinkle ridges display en echelon patterns, which imply their formation by strike-slip shear deformation with basement-involved strike-slip faulting. This hypothesis assumes the ridges to represent folds. While agreeing that the wrinkle ridges are likely generated by folding, Rahn (1971) questions Tjia's (1970) strike-slip interpretation. Rahn instead suggests that the lunar wrinkle ridges may have been induced by gravitational sliding. The model envisioned by Rahan, schematically shown in Fig. 1A and implying a thin-skinned origin of the ridges, is similar to the later model of Cassanelli and Head (2019) proposed to explain the formation of wrinkle ridges in the central Tharsis region of Mars. Cassanelli and Head (2019) postulate that the decollement follows an ice layer, which was overlain by sequentially emplaced lava beds (see the evolutionary stage 1 to state 3 in Fig. 1B).

An alternative view of the wrinkle-ridge formation appeals for igneous processes (e.g., Fielder, 1961). Strom (1972) best articulates this hypothesis by showing that some lunar wrinkle ridges exhibit lava-flow-like landforms best interpreted as shallow-extrusive igneous bodies. Strom (1972) envisions that the related wrinkle-ridge arches were created by the emplacement of elongated laccolith bodies (Fig. 1C), which are sourced from crustal-scale, deep-seated, preexisting fractures formed by earlier impact and tectonic processes. Strom (1972) further suggests that the secondary crenulated ridges are extrusive volcanic landforms emerging from tensile fractures along the ridge crests (also see Guest, 1971).

Based on detailed mapping and satellite-image analysis, Bryan (1973) shows that his mapped lunar wrinkle ridges consistently cut across lava-flow-like landforms. This observation rules out the laccolith-dome model of Strom (1972) as a general cause of lunar wrinkle-ridge formation. Mapping by Howard and Muehlberger (1973) simultaneously reaches the same conclusion. The close association of the mapped lunar wrinkle ridges with ridge-bounding scarps leads Howard and Muehlberger (1973) to interpret the ridges and ridge-bounding scarps as folds and thrusts above a decollement. The Howard and Muehlberger (1973) hypothesis, schematically shown in Fig. 1D, is perhaps the first that explicitly invokes the thin-skinned deformation as the cause of wrinkle-ridge formations in the solar system. Similar decollement models for wrinkle-ridge formation on Mars are also proposed (Watters, 1988; Watters, 1991), In Watters (1988), decollement folding is considered to have occurred either during or after lava emplacement (Fig. 1F). Watters (1991) envisions that the martian fold decollement zone follows a lava-covered regolith layer (see the sketch in Fig. 1E based on the model envisioned by Watters, 1991; also see Mangold et al., 1998).

In contrast to the decollement models mentioned above, Zuber and Aist (1990) and Allemand and Thomas (1995) argue that wrinkle-ridge formation on Mars can be explained by crustal-scale thrusting (i.e., thick-skinned deformation), and the fold-generating thrust systems may also involve backthrusts (Fig. 1G). Plescia and Golombek (1986) propose that deep-skinned wrinkle ridges on the Moon, Mercury, and Mars may represent thrust-related fault-bend or fault-propagation folds observed widely on Earth (Fig. 1H). A key prediction of the thick-skinned molde is that the blind thrusts below the wrinkle ridges extend downward to and merge into the ~30-km deep flat decollement zone (e.g., Allemand and Thomas, 1995). As predicted by the classic fault-bend fold model (Suppe, 1983), motion along 30-km deep thrust ramps dipping at 30 degrees would have produced uplifts with their horizontal dimensions equivalent to the horizontal length of the ramps at ~ 52 km. A variation of the thick-skinned thrusting model is the addition of backthrusts above the main thrusts that produced the wrinkle ridges by Okubo and Schultz (2004). In their model, motion on the primary thrust generates the broad arch represented by the wrinkle ridge above; meanwhile, secondary branching thrusts create smaller crenulated ridges (Fig. 1I). The mechanical plausibility of basement-involved thrusting for wrinkle-ridge formation is further demonstrated by Montési and Zuber (2003); their work shows that wrinkle ridges were likely developed as folds involving the upper 20 to 40 km of the upper crust.

Note that the thin-skinned model requires the presence of an un-deformation footwall below the decollement that bounds folds above. To our knowledge, exactly how the footwall is shortened during the folding event has never been discussed in the literature. In contrast, the thick-skinned model does not require an additional mechanism to absorb the footwall shortening, because rocks below the decollement are ductile lower crustal rocks below the brittle-ductile transition (Allemand and Thomas, 1995; Mueller and Golobek, 2004). Observations supporting the thin-skinned model (i.e., decollements are within the brittle upper crust) include short dimensions (i.e., only a few km wide) of wrinkle ridges (Karagoz et al., 2022b), while observations supporting the thick-skinned models on Mars come from unidirectionally dipping thrusts that bound parallel wrinkle ridges on sloping terrain on Mars (Golombek et al., 2001). More recently, Andrews-Hanna (2020) uses a Monte Carlo boundary-element model to show that the topographic profiles of wrinkle ridges, if they still represent the original fold shapes, can be explained by a range of subsurface thrust configurations involving thin- and thick-skinned styles of deformation.

From the above literature review raises two issues. First, the models for the formation of wrinkle ridges are all based on local geological observations. Because of this, it is possible that wrinkle ridges could have been created by multiple mechanisms leading to similar ridge shapes. Second, in all the quantitative models for wrinkle-ridge formation, topographic profiles are regarded as representing the original fold shapes that can be used for inverting the geometry, slip magnitude, and decollement depth of the inferred subsurface thrusts (e.g., Schultz, 2000; Mueller and Golombek, 2004; Andrews-Hanna, 2020; Watters, 2021 Karagoz et al., 2022b; cf. Mège and Reidel 2001). We note that in the Tharsis region of Mars, where this study is conducted, protracted volcanism since ~3.8 Ga has been documented (e.g., Carr, 1973; Neukum et al., 2004; Baptista et al., 2008; Hauber et al., 2009; Richardson et al., 2013, 2021; Mouginis-Mark et al., 2022). Additionally, open-water fluvial processes (Mangold and Ansan, 2006; Mangold et al., 2008; Ansan and Mangold, 2006, 2013), glacial deposition and erosion (e.g., Fueten et al., 2011; Mège and Bourgeois, 2011; Gourronc et al., 2014; Brunetti et al., 2014; Dębniak et al., 2017; Grau Galofre et al., 2020; Yin et al., 2021), and eolian processes (Ward et al., 1985; Edgett, 1997; Bridges et al., 2010; Berman et al., 2011) have all been documented in the Tharsis region. Hence, whether the post-ridge geological processes have significantly modified the ridge morphologies requires a detailed and systematic assessment.

2. Regional Setting of the Study Area

The study area is located in the Solis Dorsa wrinkle-ridge field of the central Tharsis rise (Fig. 2). The area is bounded by Sinai Planum, Valles Marineris, Thaumasia Planum, and Solis

Planum, respectively (Fig. 2). The Tharsis rise is the youngest, topographically highest volcanic-tectonic province on Mars that hosts the tallest shield volcanoes on the planet (Smith et al., 1999; Solomon et al., 2005; Tanaka et al., 2014). The interpreted tectonic history of the Tharsis rise has been focused on (1) whether its topography was created rapidly in the Late Noachian at ~3.8 Ga (Phillips et al., 2001; Carr and Head, 2010; Cassanelli and Head, 2019) or slowly and continuously since ~3.8 Ga to the present (Zuber, 2001; Neukum et al., 2004; Solomon et al., 2005; Nimmo and Tanaka, 2005; Zhong, 2009; Golombek et al., 2010; Yin et al., 2012a; Tanaka et al., 2014) and (2) the relative importance of tectonic processes, igneous process and some forms of their combinations (Solomon and Head, 1982; Neukum et al., 2004; Zhong, 2009; Hauber et al., 2009; Mangold et al., 2010; Yin et al., 2012a; Yin et al., 2012b; Tanaka et al., 2014; Richardson et al., 2013, 2021; Bouley et al., 2018; Cassanelli and Head, 2019; Mouginis-Mark and Wilson, 2019). The igneous-process models for Tharsis formation advocate the role of mantle upwelling and the resulting partially melting in contributing to magmatic underplating and crustal thickening of the Tharsis region (Carr, 1974; Wise et al., 1979; Mège and Masson, 1996a, 1996b; Harder and Christensen, 1996; Baker et al., 2007; Dohm et al., 2007; Zhong, 2009). Alternatively, juvenile-crust formation through diking (Lillis et al., 2009) or thick (5-10 km) deposition from the top (Solomon and Head, 1982) have also been proposed as crustal thickening and uplift mechanisms for the Tharsis development. Mantle melting induced by giant impacts as the cause of magmatic underplating or volcanic eruptions have also been suggested (Solomon and Head, 1982; Reese et al., 2004; Golabek et al., 2011). The volcanic-loading models such as that proposed by Solomon and Head (1982) predict surficial compressional deformation around the center of the load and extension across the rim regions of the loads. In contrast, the magmatic underplating model predicts upward doming leading to extension in the center of the subsurface load and radial compression across the rim zone of the underplating center (e.g., Tanaka et al., 1991; Banerdt et al., 1992).

Tectonic processes may have also been responsible for the formation of the Tharsis rise and the early Mars topography (Stevenson, 2001). For example, Sleep (1994) proposes the western half of the Tharsis rise was created by the construction of a magmatic arc. Expanding on this idea, Yin (2012a) constructs a primitive plate-tectonics model that predicts the Tharsis formation was created mainly by diking during local slab rollback. This model predicts local thermal-boundary-layer recycling (Yin et al., 2012a), horizontal translation of rigid blocks (Yin, 2012b; Dohm et al., 2018), and compressional tectonics across the eastern Tharsis rise as a result of retro-arc compression (Yin, 2012a). The formation of the Tharsis rise has also been related to mantle upwelling induced by convective removal of the Tharsis mantle lithosphere (Scott and Wilson, 2003). Additionally, the development of a stationary hotspot (Carr, 1974) or a migrating mantle-upwelling sheet (Zhong, 2009) may have caused the formation of the Tharsis rise.

Examining Viking images leads to the recognition of wrinkle ridges on Mars (Wilhelms, 1974; Carr et al., 1977; Greeley and Spudis, 1978a; Greeley and Spudis, 1978b; Lucchitta, 1978). Detailed mapping allows Lucchitta and Klockenbrink (1981) to classify martian wrinkle ridges into two types: Type-1 ridges have linear traces and occur exclusively in smooth-plain terrain, and Type-2 ridges have curvilinear traces with an anastomosing pattern that occur exclusively in cratered terrain. Lucchitta and Klockenbrink (1981) attribute the formation of Type-1 ridges to horizontal shortening and Type-2 ridges to differential uplifts during high-angle faulting.

Plescia and Golombek (1986) also conclude that martian wrinkle ridges have been created by tectonic shortening and consider them expressions of thick-skinned, thrust-related fault-bend and fault-propagation folds (Fig. 1G) (also see Mueller and Golombek, 2004). Their interpretation is supported by the similar morphology of martian wrinkle ridges with a suite of thrust-related folds on Earth. Several researchers show that scarps bounding wrinkle ridges appear to offset crater rims and crater floors at a few localities in the Tharsis region (Allemand and Thomas, 1995; Karagoz et al., 2022a, Karagoz et al., 2022b). Cole and Andrews-Hanna (2017) interpret a ridge-forming landform cutting obliquely across beddings exposed on a steep trough wall of Valles Marineris as a thrust zone, because it can be projected below a nearby wrinkle ridge.

The driving mechanisms for the formation of wrinkle ridges on Mars have been attributed to volcanic loading (Phillips and Lambeck, 1980), cooling of the planet (Schubert et al., 1992; Nahm and Schultz, 2011; Andrews-Hanna, 2020), and backarc compression for the eastern Tharsis region (Yin, 2012a). Globally, crater dating shows that wrinkle ridges on Mars were formed in the Early Hesperian (3.7-3.4 Ga) (Ruj and Kawai, 2021).

3. Data and Methods

Regional topographic maps were constructed by blending High Resolution Stereo Camera (HRSC) data collected by the Mars Express orbiter with the Mars Orbiter Laser Altimeter (MOLA) data (200 m/pixel) collected by the Mars Global Surveyor orbiter (Fergason et al., 2018) (Fig. 2). The blended digital elevation model (DEM) was superposed over a global mosaic of Thermal Emission Imaging System (THEMIS) daytime-infrared images at a resolution of 100 m/pixel (Edwards et al., 2011; Fergason et al., 2018) or a global mosaic of Context Camera (CTX) images (Dickson et al., 2018) at a resolution of ~6 m/pixel obtained by the Mars Reconnaissance Orbiter (Malin et al., 2007). We performed the above data superposition using the Java Mission-planning and Analysis for Remote Sensing GIS software package (JMARS) of Christensen et al. (2009).

Our geomorphologic mapping was conducted using HiRISE images at a resolution of 25 cm/pixel. The final geomorphological map was drafted using Adobe Illustrator.

Interpreting the formation processes of a mapped landform can be highly non-unique, which is best illustrated by the aforementioned debate on whether the Valles Marineris region has ever experienced glaciation. To enhance the likelihood of the interpreted formation mechanism for an observed landform assemblage, we adopt in this study a landsystem approach (e.g., Evans, 2003; Yin et al., 2021; Chen and Yin, 2022). Specifically, we seek a landsystem model capable of explaining (1) the relationship between morphology and sedimentology of individual landforms and (2) the formation of all spatially and temporally related landforms in the assemblage by a single geologic process. The landsystem approach has been proven successful for geomorphologic research on Mars in the work of Head et al. (2010), Gallagher and Balme (2015), Butcher et al. (2016, 2017), and Dębniak et al. (2017) , to name a few. To further support our landsystem approach, we use throughout this study well-understood and well-documented Earth analogues to guide our interpretations.

4. Results

4.1 Geological Context of the Solis Dorsa Wrinkle-Ridge Field

Solis Dorsa is a northeast-trending oval-shaped basin that is ~800 km wide in the northwest-southeast and 1200 km long in the northeast-southwest direction (Fig. 2). The first-order cross-cutting relationships among the major topographic features can be deciphered using the DEM map and the nighttime temperature map of the region (Figs. 2B and 2C). The oldest terrain is the eastern highland region of Thaumasia Planum; its western boundary marked (feature 1 in Fig. 2C) truncates east-northeast trending darker- and lighter-toned bands in the Solis Dorsa region (feature 2 in Fig. 2C), which is together referred to as the “banded terrain” in this study. The highland terrain itself is cut by linear grooves that trend northeast (feature 3a in Fig. 2C), northwest (feature 3b in Fig. 2C), and east (feature 3c in Fig. 2C), respectively. The grooves are in turn superposed by north-trending wrinkle ridges in the highland terrain (features 4a, 4b, and 4c in Fig. 2C). East-northeast-trending darker-toned stripes (feature 5 in Fig. 2C) in the banded terrain are also superposed by the north- and northeast-trending wrinkle ridges (feature 6 in Fig. 2C).

Two types of craters occur in the study area: (1) rampart craters characterized with layered viscous-flow-like ejecta-blanket deposits (feature RC and yellow lines that outline the extent of the impact deposits in Fig. 2C), and (2) non-rampart-like craters characterized with simple rim ridges and circular ejecta-blanket deposits (feature NR in Fig. 2C). The largest rampart crater ejecta-blanket deposits (feature 7 in Fig. 2C) in the banded terrain is superposed over the nearby wrinkle ridges (feature 6 in Fig. 2C). We note that rampart craters occur throughout the banded terrain. However, this is not the case for the highland terrain in which craters in the highest topographic region are non-rampart types: they show well-defined central uplifts and rim ridges, but they lack viscous-flow-like ejecta-blanket deposits. Sinuous, finger-shaped scarps are present in the highland terrain, but there are no obvious craters that can be correlated with these features (white dashed lines in Fig. 2C).

The detailed relationship between grooves in the highland terrain and wrinkle ridges is further illustrated in a zoom-in image in Figs. 3. Here, a northwest-trending linear groove (feature 1 in Fig. 3A) is terminated and superposed by a northeast-trending wrinkle ridge (feature 2 in Fig. 3A). Also shown in Fig. 3A is a curvilinear, grooved pit chain (feature 3) that cuts across the same wrinkle ridge shown as feature 1 in the figure. Viscous impact ejecta deposits (feature 4 in Fig. 3A) derived from a rampart crater (feature 5 in Fig. 3A) is cut by a set of northwest-trending grooves (feature 6 in Fig. 3A). Fig. 3A also shows younger craters postdating the grooves (feature 7) and wrinkle ridges (feature 8). Fig. 3B as a zoom-in view shows that the steep walls of a set of northeast-trending grooves (features 1 and 2) are cut by a north-trending, arcuate-shaped, wrinkle ridge (feature 3); this again supports the groove formation predates wrinkle-ridge formation.

A more complicated relationship between grooves and wrinkle ridges is shown in Fig. 3C. Here, a north-trending wrinkle ridge (feature 1) splits into three shorter ridges (features 2a, 2b, and 2c) aligned obliquely in an en echelon pattern. The ridge system cut across an east-trending groove that displays an apparent right-separation offset (feature 3). The right-separation and the en echelon pattern of the minor terminating wrinkle ridges are consistent with right-slip shear as shown in Fig. 3C. Superposition of a younger wrinkle ridge (feature 4) over an older east-trending groove (feature 5) is also in Fig. 3C.

The east-northeast-trending bands with eastward pinch-out terminations (feature 5 in Fig. 2C) are broad ridges (feature 1 in Figs. 4A and 4B) that are 40-50 km wide and 40-80 m higher than the surrounding background plains (Fig. 4C). The subtle, broad east-northeast-trending ridges are superposed by north and northeast-trending wrinkle ridges (feature 2 in Figs. 4A and 4B).

In summary, the following older-to-younger sequence of landform-development events can be deduced from the cross-cutting relationships shown in Figs. 2-4: (1) the development of the highland terrain in Thaumasia Planum, (2) the formation of northeast-, northwest-, and east-trending grooves likely representing extensional structures, (3) the emplacement of east-northeast-trending lava flows, (4) the formation of wrinkle ridges that are superposed on top of (a) the highland terrain, the lava-flow terrain, and (c) the earlier formed extensional structures, and (5) rampart craters with viscous-flow-like, layered, ejecta blankets.

4.2 Morphologies and Geological Context of the Wrinkle Ridges in the Study Area

A total of 19 wrinkle ridges can be recognized in the central area of the 800-km wide Solis Dorsa basin (Figs. 5A and 5B). In map view, individual ridges are 350 km to 400 km long and 10-20 km wide. The ridges display arcuate and convex-eastward traces (Fig. 5A) and occur on both the western and eastern slope of the Solis Dorsa basin while maintaining the same convex geometry (Figs. 5A and 5B). In cross-section view, the center-to-center distance of the ridges mostly lie between 50 km and 70 km. The amplitudes of the ridges vary from ~100 m to ~250 m (Figs. 5B and 5C).

In the study area, we mapped 6 wrinkle ridges numbered as wr1 to wr6 in Figs. 5A and 5B. The geological context of the six ridges is defined by mapping over a CTX image superposed over a THEMIS nighttime temperature map. Our mapping reveals the following landform units (Fig. 6): (1) craters that do not have direct cross-cutting relationships to the wrinkle ridges (unit ct), (2) craters that postdate the wrinkle ridges (unit ct2), (3) wrinkle ridges (unit wr), (4) craters with their impact ejecta-blanket deposits cut by ridge-bounding faults (unit ct1), (5) darker-toned bands with digitate margins (unit bd), and (6) light-toned background terrain that hosts the darker-toned bands (unit pl). Examples of craters postdating and predating wrinkle ridges are shown in Fig. 7.

Excluding the overlapping images, a total of 16 HiRISE images are available in the study area for detailed examination of landforms associated with the wrinkle ridges and inter-ridge plains. We refer to each HiRISE image strip as an investigation site, which is numbered from 1 to 16 (Fig. 6A). Our work shows that the surface of the study area is dotted by boulders and breccias. Fig. 8 shows the occurrence of boulders on top of wrinkle ridges surrounded and/or draped over by variable amounts of finer-grained materials. The boulder-bearing surfaces have diverse morphologies ranging from undulating, pitted, to smooth (Fig. 8). The smooth boulder-bearing surfaces locally display northwest-trending linear grooves and ridges; ridges are locally defined by linear alignment of meter-scale boulders (Fig. 8). These linear features are together referred to as striations for their resemblance to striations on fault surfaces.

Meter-scale boulders are also scattered across the plains between wrinkle ridges (Fig. 9). Linear landforms composed of light-toned and fine-grained materials with grain sizes below the resolution of HiRISE images occur widely on the surface of the boulder-bearing inter-ridge plains (Fig. 9). These linear features are likely eolian bed forms, which differ from the linear grooves and ridges on top of the wrinkle ridges in that (1) the boulders are not aligned and no well-defined grooves next to the light-toned ridges, and (2) the striations on ridge tops trend northwest whereas the light-toned ridges on the plains trend northeast.

The largest craters in the inter-ridge plains display viscous-flow-like, layered ejecta-blanket deposits (Figs. 10A, 10B, 10D, and 10E). The exposed crater walls on the inter-ridge plains show well-defined bedding (Figs. 10C and 10F). One of the largest craters on top of the wrinkle ridges is shown in Figs. 10G and 10H. This crater differs from those exposed on the inter-ridge plains in that (1) it does not display viscous-flow-like ejecta deposits, (2) the crater wall displays only three well-defined bedding horizons and the rest appears to be massive-textured materials, (3) the crater floor exhibits a lobate ridge with a northward-concave shape that requires a northern source, and (4) no landslide scarps are present on the northern crater wall that rules out the lobate ridge to have been resulted from mass wasting.

The wrinkle ridge traversed by investigation sites 2, 3, and 4 (Fig. 6) display several types of lobate landforms. The western edge of the ridge is marked by a lobate apron sheet (Figs. 11A and 11D), a lobate taper (Figs. 11B and 11E), and a lobate ridge (Figs. 11C and 11F), respectively. The lobate apron sheet is superposed on top of the wrinkle ridge (Fig. 11A). Similarly, the lobate taper composed of massive-textured boulder-bearing materials is piled on top of the flat wrinkle-ridge surface (Fig. 11B). Less prominent is the lobate ridge that lies on top of the wrinkle-ridge surface (Fig. 11C). The above superposition relationships suggest that the lobate landforms postdate the formation of the wrinkle ridge. The eastward-convex shapes of the lobate taper and lobate ridge require eastward movement of the taper/ridge materials. However, no candidates are present as the pushers as these landforms are against the flat inter-ridge plains to the west (Figs. 11B and 11C). The eastern front of the same wrinkle ridge is also marked by lobate landforms, which are expressed arcuate-shaped, flow-front-like steep limbs (Figs. 11A-11C). In all three cases, the steep ridge fronts transition to the flat ridge tops through round-shaped hinge zones (Figs. 11A-11C).

Boulder-bearing ridges occur widely in the study area. The best exposed ridge network is at site 7 on the inter-ridge plains (Fig. 12). The ridges display crude dendritic-network patterns with ridges merging and/or converging northeastward. Zoom-in views show that the ridges are composed of boulder materials that are locally layered dipping to the northeast in the direction of ridge convergence (Figs. 12B-12D).

4.3 Detailed Mapping of Site 11

Investigation site 11 is covered by HiRISE image ESP_018071_1540 at the resolution of 50 cm/pixel. We mapped this site systematically (Fig. 13) in order to establish the spatial distribution of secondary landforms associated with larger wrinkle ridge and the chronological relationships between the secondary landforms and the hosting wrinkle ridges. We divide the map area into three geomorphological assemblages: the northern plains, the wrinkle-ridge, and the southern plains.

Northern Plains Assemblage. This assemblage consists of a single unit: rough-surfaced plains terrain (unit rf in Fig. 13B). This unit is characterized by patches of flat, higher-elevation mesa surfaces (feature 1 in Fig. 14A) that are surrounded by depressions of similar sizes (feature 2 in Fig. 14A). This terrain also exposes degraded, polygonal-shaped craters characterized by breached crater rim ridges (feature 1 in Fig. 14B) with flat crater floors (feature 2 in Fig. 14B). Knobs surrounded by smooth-surfaced plains are also present (feature 3 in Fig. 14B). Finally, viscous-flow-like landforms without clear association of nearby impact craters occur locally in this terrain (feature 4 in Fig. 14B). Even the crater with a better preserved rim ridge has a smooth-surfaced flat crater floor (feature 1 in Fig. 14C) similar to those of the degraded craters. This observation implies that the process responsible for flat crater-floor development occurred after the emplacement of the two types of craters. The wall of the crater shown in Fig. 14C exposes meter-sized boulders without discernible layering (feature 1 in Fig. 14D). The rim ridge and the wall of the crater are superposed by northwest-trending linear ridges and grooves (feature 2 in Fig. 14D). The smooth-surfaced material on the crater floor embays the crater-wall boulders (feature 3 in Fig. 14D), suggesting that the formation of the flat crater floor postdates the formation of the crater. The most characteristic feature in the rough-surfaced plains terrain (feature 1 in Figs. 14E-14G) are bounder piles of various shapes that are superposed by fresh (feature 2 in Figs. 14E-14G) and degraded craters (feature 3 in Figs. 14E-14G).

Wrinkle-ridge Assemblage. This assemblage displays the most diverse landforms in the mapped area. On the northern and southern margin of the wrinkle ridge are the northern and southern foothill terrains (unit fhN and unit fhS in Fig. 13B), which are characterized by (1) scarp-bounded, uneven-surfaced, wrinkle-ridge-parallel highland strips, and (2) discontinuous, round-topped ridges that are parallel or oblique to the main trend of the wrinkle ridges. The main part of the wrinkle ridge is divided by a curvilinear-ridge terrain (unit cr in Fig. 13B) into the northern and southern smooth-surfaced ridge terrains (unit srN and unit srS in Fig. 13B). A lumpy-ridge terrain (unit Lr in Fig. 13B) lies between the northern rough-surfaced plains terrain and the northern smooth-surfaced ridge terrain. Finally, irregularly shaped depressions with flat floors and steep walls (unit ird in Fig. 13B) are present in the northern part of the wrinkle ridge.

The landform units mentioned above are superposed by (1) linear and curvilinear scarps best developed along the northern and southern margins of the wrinkle ridges, although some isolated scarps also occur on top of the smooth-surfaced ridge terrain (purple lines in Fig. 13B), and (2) sinuous, sharp-crested ridges (orange lines in Fig. 13B).

Fig. 15A shows the locations of zoom-in images of the wrinkle-ridge landform assemblage. Fig. 15B shows a scarp-bounded, uneven-surfaced, highland strip in the northern foothill terrain (feature 1). A zoom-in view of the highland strip shows that it exposes meter-sized boulders expressed as dark- and light-toned dots (feature 1 in Fig. 15C). The base of the southern scarp in Fig. 15C displays eolian bedforms (feature 2). Fig. 15D shows the curvilinear, sharp-crested ridges on top of the wrinkle ridge, whereas Figs. 15E-15G are zoom-in views of the ridges that expose massive-textured boulder materials. Note that dendritic patterns of ridge networks are indicated in Fig. 15 E (feature 1), which are embayed by the younger, smooth-surfaced mantling material (feature 2). Materials making up the wrinkle ridge are exposed by crater walls (Figs. 15H-15J), which do not show clearly defined layering. The flat ridge top shows distinctive regions with (feature 1 in Fig. 15K) or without (feature 2 in Fig. 15K) the fine-grained mantling materials.

The southern foothill terrain has a transitional boundary to the southern plains assemblage as shown in Fig. 16A. Key morphological features of the southern foothill terrain are shown in Figs. 16B-16E. Figs. 16B-16C shows a foothill, characterized by a sharp crest and bounded by a steep south-facing scarp (feature 1), bounds a smooth-surfaced basin to the north (feature 2) that lies at higher elevation than the plains (feature 3) south of the sharp-crested ridges. The sharp-crested ridges in the foothill terrain is locally highly curvilinear and perched on a south-facing slope (feature 1 in Fig. 16D). Both the ridge and the hosting slope expose meter-sized boulders (feature 2 in Fig. 16D).

Irregularly shaped mound complexes are also present in the southern foothill terrain (feature 4 in Fig. 16B). A zoom-in view of a mound complex shows a sharp-crested ridge (feature 1 in Fig. 16E) truncates a circular depression resembling a degraded impact crater (feature 2 in Fig. 16E). The younger ridge material is also emplaced into the crater basin crater (feature 3 in Fig. 16E). Note that the geomorphological relationship shown in Fig. 16E is similar to those shown in Fig. 11, which resemble gravel piles pushed up by bulldozers. Here, we refer to this class of landforms as “bulldozed-pile-like” features.

Note that the sinuous ridge in the southern foothill terrain is remarkably similar to the map-view traces of the ridge shapes in the curvilinear ridge terrain (Fig. 16I; cf. Figs. 15D-15G). A zoom-in image shows that the ridge is composed of layered boulders (Fig. 16J), similar to the internal layered structure of a boulder ridge on top of another wrinkle ridge as shown in Fig. 12C.

Southern Plains Assemblage. This assemblage consists of a smooth-surfaced plains terrain (unit sf in Fig. 13B) and a rough-surfaced plains terrain (unit rf in Fig. 13B). The smooth-surfaced plains are characterized by the presence of light-toned mantling materials that fill the lowland regions including craters (feature 1 in Fig. 16F). In contrast, the rough-surfaced plains terrain is free of the mantling materials despite its occurring next to the smooth terrain (feature 2 in Fig. 16F). The rough-surfaced plains expose meter-scale bounders on a surface that is dotted by degraded craters (Fig. 16G), whereas the smooth-surfaced plains lack the appearance of boulders due to the presence of the mantling materials (Fig. 16H).

Striations and Scarps (Fig. 17). The northwest-trending striations mapped in this study are expressed as linear, regularly spaced, parallel boulder ridges (feature 1 in Fig. 17B) and flat-floored grooves (feature 2 in Fig. 17B). The surface that hosts the striations appears to have been polished, which is expressed by the occurrence of flat-rimmed craters (feature 3 in Fig. 17B).

The northwest-facing scarp (feature 1 in Fig. 17C) bounding a northern foothill of the wrinkle ridge (see Fig. 17A for location) against the northern plains truncates an accurate ridge on the flat top of the foothill (feature 2 in Fig. 17C). This relationship indicates the scarp formed after the foothill.

The foothills along the northern margin of the wrinkle ridge are composed of boulders (Fig. 17D). The scarp that bounds the boulder hill in Fig. 17D (feature 1) is locally collapsed due to mass wasting, forming a talus pile that buries the scarp below (feature 2).

Fig. 17E shows a crater rim ridge (feature 1) that is truncated by an east-facing scarp (feature 2). Note that the scarp material intrudes into the crater basin (feature 3 in Fig. 17E). Also note that the impact deposits recognizable below the scarp (feature 4 in Fig. 17E) are missing on top of the flat-topped ridge above the scarp.

Fig. 17F shows a flat-floored depression (feature 1) is truncated by an east-facing scarp (feature 2). The scarp exposes parallel linear ridges and grooves (feature 3), which may represent inclined layers that contain boulders.

Chronological Sequences of Geological Events. Based on the geological mapping, we discuss the possible sequence of geological events in the study area. The light-toned mantling material has filled both degraded and relatively well-preserved crater basins in the northern plains terrain (Fig. 14). In contrast, the mantling material in the southern plains only covers the smooth-surfaced plains terrain, where craters and depressions are filled by this material (Figs. 16F and 16H). The rough-surfaced plains terrain, on the other hand, lacks the mantling material although it could lie (e.g., feature 2 in Fig. 16F) directly next to the smooth-surfaced plains terrain covered by the mantling material (e.g., feature 1 in Fig. 16F). Note that sharp boundaries between regions with and without the mantling material also occur on top of the wrinkle ridge (see Fig. 15K). There are two possible interpretations on the age relationship between the smooth-surfaced and rough-surfaced terrains in the plains and ridge regions. First, the formation of the rough-surfaced terrain occurred after the emplacement of the mantling material. However, the similar elevation and a lack of a clear topographic break between the two terrains makes this interpretation unlikely. Second, the emplacement of the mantling material is spatially heterogeneous; areas covered by the materials display a smooth-surfaced texture whereas areas not covered show the original rough-surfaced texture. Because the mantling material occurs on top of the ridge and on the ridge-bounding plains, its emplacement must postdate the wrinkle-ridge formation.

Geomorphological features that formed after the wrinkle-ridge formation include (1) the set of northeast-trending linear grooves on top of the wrinkle ridge (black lines shown in Fig. 13B), and (2) sharp-crested, curvilinear, and locally dendritic-patterned ridge networks (orange lines in Fig. 13B). Note that the curvilinear-ridge terrain truncates the northwest-trending linear grooves (Fig. 13B), which implies that the emplacement of the boulder-bearing, sharp-crested, curvilinear ridges occurred after the wrinkle-ridge surface was grooved. Also note that the grooves are filled by the mantling material, which implies that the mantling event postdates the grooving event. Because the curvilinear, sharp-crested ridges are embayed by the younger mantling material, the ridge formation predates the mantling event.

In summary, our mapping reveals the following sequence of event in the study area: (1) formation of the main wrinkle ridges and its foothill terrains, (2) formation of the northwest-trending grooves on top of the wrinkle ridge, (3) formation of boulder-bearing, curvilinear, sharp-crested ridges, and (4) emplacement of the heterogeneously distributed mantling material.

Deformation and Erosion Modification. Our work indicates that the scarp formation postdates their bounded ridges; their truncation relationships with early landforms such as curvilinear ridges and impact craters require the scarps to represent fault-like deformation structures. The occurrence of parallel ridges and grooves on a polished surface suggests that the surface of the mapped wrinkle ridge has been modified by younger erosional events capable of shaping the alignment of meter-scale boulders.

5. Discussion

Our regional and local geologic mapping and a systematical analysis of HiRISE images and HRSC topographic data lead to the following first-order observations.

1. The northeast-trending wrinkle ridges with reliefs of 100-300 m (Fig. 5) in the Solis Dorsa area are superposed on top of older, east-trending, lower-relief (<30 m) ridges (Fig. 4). The digitate margins, sinuous and winding traces, and eastward converging terminations (Figs. 3, 4, and 6) all support the older east-trending ridges to have been formed by basalt-lava flow as envisioned by Tanaka et al. (2014).

2. In map view, individual wrinkle ridges display consistent eastward convex shapes (Fig. 5A), which implies eastward transport direction of the landform system as it represents a thin-skinned fold-and-thrust belt (e.g., Allemand and Thomas, 1995; Karagoz et al., 2022a, 2022b; cf. Mueller and Golombek, 2004).

3. In cross-section view, the wrinkle ridges occur on the two sides of the Solis Dorsa basin with basin margins sloping to the east in the west and to the west in the east (Fig. 5B).

4. Wrinkle ridges either cut across craters (Fig. 7A) or are cut by craters (Fig. 7B).

5. The surface of the wrinkle ridges and their bounding plains expose massive-textured, meter-sized boulders (Fig. 8).

6. The boulder-bearing surfaces are locally superposed by parallel, regularly spaced, boulder-bearing ridges and grooves (Figs. 8C, 8E, 8G, 8H, and 8K; Fig. 17K).

7. Craters with diameters greater than 4-5 km display viscous-flow-like, layered ejecta deposits (Figs. 7, 10A, 10B, 10D, and 10E).

8. The margins of wrinkle ridges locally display flow-like fronts in cross-section view and lobate-apron-like shapes in map view (Fig. 11).

9. A distinctive type of landforms is also recognized in this study, which is characterized by their shapes resembling debris piles pushed by bulldozers (Figs. 11 and 16E).

10. Wrinkle ridges and their bounding plains are locally superposed by sinuous, sharp-crested, and boulder-bearing ridges (Figs. 12, 16C, 16D, and 16I). The ridges locally expose inclined layers (Figs. 12D and 16J).

11. Most wrinkle ridges and their bounding plains are draped over by a light-toned, smooth-surfaced mantling material. However, the mantling is not spatially uniform, with some regions directly next to mantled terrain show no signs of mantling (Fig. 16F).

12. Our regional (Fig. 6B) and local mapping (Fig. 13B) leads to the following interpreted older-to-younger sequence of events for the landscape evolution of the Solis Dorsa wrinkle ridge field:

a. The formation of the Thaumasia highlands.

b. Formation of linear grooves across the highlands.

c. Emplacement of the east-trending ridges interpreted as lava flows that were stopped in the east by the Thaumasia highlands.

d. Development of boulder-bearing surfaces on top of the flows.

e. Formation of the wrinkle ridges and coeval impacts that display rampart-style ejecta-blanket deposits.

f. Development of striated surfaces over wrinkle ridges and inter-ridge plains. Degraded craters could also have been formed during this time.

g. Development of sinuous, sharp-crested, and boulder-bearing ridges locally exposing inclined beds.

h. Spatially heterogeneous distribution of the mantling material that fills older craters.

i. The formation of modern eolian landforms best expressed as dune fields in lowland regions and depressions.

Any models for the formation of wrinkle ridges and their subsequent modifications in the Solis Dorsa region must account for the above observations and a self-consistent geologic history as constrained by our mapping.

6.1 Origin of Surficial Boulders

Meter-scale boulders that occur everywhere in the regional study area could have been generated by three possible processes: (1) impact gardening that results in the formation of a surficial boulder-bearing regolith layer (e.g., Hartmann et al., 2001; Warner et al., 2017) (Fig. 18A), (2) autobrecciation of volcanic flows (e.g., Parsons, 1969; Smellie et al., 2011) (Fig. 18B), and (3) glacial tills (e.g., subglacial stone pavement of Hicock, 1991 and glacial-boulder pavements of Atchison, 2013) (Fig. 18C).

The impact gardening model predicts that boulders in the study area should have sizes from < 1 m to >100 m, which has been observed on Mars (i.e., the mega-breccias of Grant et al., 2008; Tornabene et al., 2013). Our observations contradict this expectation; they show instead that the boulder sizes are limited to an upper size limit of ~5 m (Fig. 8). Hence, invoking the impact gardening mechanism would require additional processes that help sort the clast sizes. For example, it is possible that our study area is located far from large craters capable of creating breccias that are 10s of meters across. But this special plea does not explain why the boulder sizes are generally similar and the upper size limit appears to be similar everywhere in such a large area that is ~300 km wide and 400 km long (Fig. 6).

Autoclastic volcanic breccias are those formed (1) within a volcanic plug, (2) at the surface by the rising and crumbling of domes and spines, and (3) within unconfined lava flows (Parsons, 1969). Flow breccias may develop on top of a lava flow, resulting in the formation of aa-type surface textures (Parsons, 1969). This interpretation is consistent with the presence of interpreted lava flows in the area. One observation this hypothesis may not be able to explain is the occurrence of rampart craters with viscous-flow-like ejecta deposits in areas where wrinkle ridges are developed. Craters with viscous-flow-like ejecta are considered to have been formed in impact-target rocks that contain ice layers (e.g., Mouginis-Mark, 1987; Weiss and Head, 2014; Cassanelli and Head, 2019 and references therein). However, the emplacement of lavas would have created steams and phreatic volcanic explosions, leading to the release of water below the lava flows (e.g., Parsons, 1969; Smellie et al., 2011; cf. Cassanelli and Head, 2019).

Debris-covered glaciers (Benn et al., 2012) can overcome all the difficulties encountered by the two hypotheses mentioned above. First, glacial transport may provide a sorting mechanism that limits the maximum clast size (Boulton, 1978). Second, the viscous-flow-like materials could have been derived from the ice layer below the debris layer as suggested by Cassanelli and Head (2019). A key difference between our debris-covered glacier model and the supraglacial-lava flow model of Cassanelli and Head (2019) is that our debris layer lies above rather than below a lava pile; our model implies post-lava glaciation, while their model requires syn-glaciation lava emplacement.

The possibility that the surficial boulder layer in the Solis Dorsa area may represent glacial deposits raises the question of whether the entire wrinkle ridges were allochthonous materials transported by glaciers or the ridges are mostly composed of the east-trending lava flows and only their surfaces are draped by a thin (<10-30 m) layer of boulders. As shown in Fig. 4A, the nighttime isothermal bands are superposed over most of the wrinkle ridges, which suggests that the major mass of the wrinkle ridges still record the thermal properties of the interpreted lava flows. Hence, we conclude the wrinkle ridges are not composed of exotic materials except their surficial layers, which are too thin to alter the thermal properties of the lava flows below.

6.2 Formation Mechanisms of Wrinkle Ridges

As reviewed in the introduction of the paper, debates on wrinkle-ridge formation have been focused on (1) igneous vs. tectonic processes, (2) thermal contraction vs. tectonic compression, and (3) crustal-scale thick-skinned shortening vs. shallow-crustal thin-skinned/decollement-facilitated shortening (see reviews by Mueller and Golombek, 2004; Watters, 2022).

Igneous mechanisms predict the wrinkle ridges to have formed above an elongated laccolith sheet, which would predict extension and formation of tensile fractures along the ridge crests (Strom, 1992). The predicted extensional fractures are not observed in this study. However, the flow-front morphology associated with many wrinkle ridges in the study area (Fig. 9) does suggest that the formation of the wrinkle ridges may have been accomplished by a ductile-deformation process rather than by a brittle faulting process. We rule out the ductile deformation to have been associated with the lava-flow emplacement because the northeast trend of the wrinkle ridges is oblique rather than perpendicular to the longitudinal east trend of the interpreted lava flows.

Thermal contraction may explain horizontal shortening across the wrinkle ridges. However, this mechanism does not explain why the wrinkle ridges have a consistent eastward-convex shape across the Solis Dorsa wrinkle field. One would also expect that thermal contraction due to magma cooling below the Tharsis rise would have generated a crustal-scale stress field leading to the formation of compressional structures with horizontal wavelengths similar to the thickness of the Tharsis crust on the order of 10s of kilometers. This expectation is inconsistent with the highly localized deformation expressed by the wrinkle ridges bounded by flat inter-ridge plains (see Karagoz et al., 2022a, Karagoz et al., 2022b). Finally, heterogeneous cooling is expected due to multiple intrusions in different times and at different locations below the Tharsis rise, which would require superposition of compressional structures with different orientations that crosscut one another. Such relationships are not observed.

Tectonic compression is a plausible mechanism as it explains the single phase of wrinkle ridge formation, their map-view shapes, and their general parallel relationship to a known mega-thrust that bounds the eastern edge of the Thaumasia highlands (Nahm and Schultz, 2011). The highly localized topography characterized by wavelengths of only a few km for the ridge width and ridge-bounding plains that have surfaces following the regional slope (Fig. 3) is most consistent with the thin-skinned decollement-fold model as suggested by Watters (1991) and advocated recently by Karagoz et al. (2022b). In contrast, the thick-skinned thrust model would predict >50 km wide wrinkle ridges for the faults that terminate at a depth of 30 km dip at or below 30 degrees. The >50-km predicted ridge width by the thick-skinned model is incompatible with the observed ridge within the study area (Fig. 5).

A major question with the thin-skinned folding model is how the basement below the decollement is shortened. On Earth, the basement is subducted below an arc such as the cases for the development of the Canadian Rocky Mountains thrust belt (e.g., Bally, 1966; Price, 198), the Zagros fold belt (e.g., Agard et al., 2011), and the Himalayan orogen (Yin, 2006). Here, we suggest that the basement below the decollement may have been subducted below the warm and ductile root of the Syria volcanic plateau, which was regarded as a magmatic arc created by slab rollback by Yin (2012b) (Fig. 19).

6.3 Origin of Boulder-Bearing, Sharp-Crested, Sinuous Ridges, Lobate Ridges, and Rampart Craters

The extreme irregularity of the sinuous ridges in map view and the lack of truncation and offset of craters along the edges of the ridges rule out the possibility that the ridges were formed by horizontal compression during the formation of the hosting wrinkle ridges. Below we consider the boulder-bearing ridges to have possibly been formed by (1) weathering-resistant lava tubes, (2) inverted fluvial channels (Williams et al., 2009; Zak et al., 2018), and (3) glacial eskers (Shreve, 1985; Clark and Walder, 1994; Warren and Ashley, 1994).

Two observations from the study area appear to be inconsistent with the lava-tube hypothesis. First, the ridges expose meter-sized boulders rather than coherent lava-flow rock mass. Second, the flanks of ridges are planar and the ridge tops are sharp-crested rather than circular that is common for lava tubes.

Sinuous boulder-bearing ridges could represent inverted fluvial channels, supported by their dendritic patterns of ridge networks similar to those exposed on Earth (Zak et al., 2018). However, the lack of ridge-terminating deltaic landforms does not favor this interpretation. Furthermore, the condition for the formation of inverted channels on Earth is that the bounding strata are fine-grained materials easily removable by erosion (e.g., Zak et al., 2018). The scattered boulders next to the boulder-bearing ridges in the study area are not consistent with this prediction. The above issue could be overcome if the deltaic deposits and the less resistant finer-grained materials originally bounding the channels were completely removed by later erosion. The most challenging issue with the inverted channel hypothesis is that the ridges dominantly trend obliquely to the local maximum slope directions, which are not consistent with them being driven by open-water flow.

Esker-like landforms have been found through Mars (e.g., Kargel and Strom, 1992; Gallagher and Balme, 2015; Butcher et al., 2021). These features do not have to follow the maximum local-slope directions because subglacial meltwater flow is driven by the gradient of hydraulic heads within the overlying ice sheet. This prediction explains why the boulder ridges trend variably across the study area regardless of the local topography (see Fig. 16D for an extreme case).

Although rare, a single lobate ridge composed of boulders are exposed on the floor of a crater exposed on top of a wrinkle ridge (Fig. 10H). The lack of an escarpment directly above the lobate ridge on the crater wall suggests that it was not formed by mass wasting process. One possible interpretation is that it represents a terminal moraine. We note that lobate ridges are closely associated with the rampart craters in the area, which has long been considered to have been the result of impacts onto ice-bearing targets (e.g., Cassanelli and Head, 2019 and references therein). Here, we suggest that the ground ice is part of the debris covered ice sheet, and the cover is represented by the widespread deposition of boulder materials after the removal of the underlying ice.

6.4 Striations, Bulldozed Debris Piles, and Irregularly Shaped Depressions

Parallel grooves and ridges defined by the linear alignment of boulders are present throughout the study area. The dominant trend of the linear landforms is northwest-southeast, which are oblique to the trend of the wrinkle ridges. The involvement of boulders with sizes as large as 5 meters rule out the ridge and groove formation to have been induced by wind action. The presence of flat-rimmed craters on the published surface that hosts the linear ridges and grooves support an interpretation that they were formed by frictional sliding of an overriding ice sheet. Moving glaciers in the study area may also explain the bulldozed-debris-pile-like landforms, which appear to have been pushed by strong indenters that are not removed. Glacial push for the formation of this class of landforms resolves this issue.

As shown in the detailed mapping area (Fig. 13B), steep-walled, flat-floored, irregular-shaped depressions locally breaching crater rim ridges are present on top of the wrinkle ridges. Although not the focus of this study, similar landforms occur widely on the inter-ridge plains. This class of landform could have resulted from melting of dead ice blocks in glacial tills during deglaciation (e.g., Brodzikowski and Van Loon, 1987; Anderson, 1989; Evans and Gooster, 2014).

6.5 Why is the Mantling Material Distributed Heterogeneously?

One of the puzzling observations in this study is the highly heterogeneous distribution of the smooth-surfaced mantling material. The filling of this material creates flat-floored craters and even partially or completely buries the older craters as described above. However, directly next to the mantled region is a terrain that displays boulder-bearing surfaces with craters showing no signs of internal fillings and mantling. Because the mantled and un-mantled areas lie on the same surface with the same elevation next to one another, it is difficult to attribute topography as the cause of this difference with the mantling material either transported by wind or falling down as volcanic ashes. The above observation, however, could be explained if glacial flours in the interpreted ice sheet are heterogeneously concentrated. Hence, the deposition of glacial flours from the higher concentration portion of the ice sheet resulted in the formation of the mantled terrains, whereas the lack of glacial flours in the overlying ice sheet left the terrain below free of mantling.

6.6 Landscape Evolution Model and Its Implications

Based on the above discussion, we propose a self-consistent evolutionary model for the landscape development of the central Tharsis rise.

Stage 1. The Thaumasia highlands was uplifted along the eastern margin of the Tharsis rise due to crustal-scale thrusting (Fig. 20A).

Stage 2. The Syria Planum highlands were created by magmatic emplacement and volcanic eruptions. This causes the westward emplacement of lava flows against the Thaumasia highlands in the east (Fig. 20B).

Stage 3. Continued east-west crustal shortening created the winkle ridges. The formation of the wrinkle ridges may have occurred when some of the lavas were still warm and viscous, creating the flow-front-like ridge morphology (Fig. 20C).

Stage 4. Regional glaciation with an overlying ice sheet atop the wrinkle ridges. This process deposited regionally extensive boulders, created striated surfaces, and formed eskers at the base of the ice sheet (Fig. 20D).

Stage 5. Deglaciation and deposition of locally highly concentrated glacial flours in the ice sheet created mantled terrain (Fig. 20E).

The most important implications from our proposed model are that:

1. The Tharsis rise region experienced volcanism first, followed by tectonic compression, which was in turn followed by glaciation. This sequence of events differ significantly from those inferred earlier (e.g., Cassanelli and Head, 2019).

2. The morphology of the wrinkle ridges in the study area may have been modified by both glacial deposition and erosion, not mentioning the later effect of wind erosion. This inference casts uncertainties in using the present-day wrinkle-ridge morphology for deducing the subsurface geometry of the thrusts below the fold-generated ridges. Erosion modification of the original wrinkle-ridge morphology means that the topographic profiles can only offer minimum values of shortening when the profile lines are straightened, and the true shortening strain could be much greater. A potential way of overcoming this issue in the future may be the use of ground-penetrating radars capable of imaging folded layers below the ridges.

3. A key implication of our model is that folding and lava emplacement may have occurred synchronously, as discussed in Watters (1988). Folding of warm and ductile lava beds helps explain the flow-front-like morphology associated with the margins of some wrinkle ridges.

Coeval shortening and volcanism during the construction of the Tharsis rise are predicted in the slab rollback model of Yin (2012b).

Despite the fact that our proposed landscape model provides a self-consistent explanation for the evolution of the central and eastern Tharsis region. The model is not unique, and as a cautious note, all competing mechanisms for generating wrinkle ridges, boulder deposits, boulder-bearing ridges, and mantled terrains remain viable. Differentiating these competing hypotheses will require more systematic investigations of wrinkle ridges in other geologic settings on Mars and other rocky bodies in the inner solar system. For example, we cannot completely rule out impact gardening and autobrecciation as boulder-generating mechanisms in the study area. Similarly, the boulder-bearing curvilinear ridges could have been formed by open-water fluvial processes if the current landscape has been altered since the ridge formation.

7. Conclusions

Geological mapping, topographic-data analysis, and examination of high-resolution satellite images at resolutions of 25-50 cm/pixel allows us to test a suite of models for the formation of wrinkle ridges in the central Tharsis region. The main result of this work is in the form of (1) a regional geomorphological map prepared using a CTX mosaic at a resolution of 6 m/pixel and (2) a local geomorphologic map prepared using a HiRISE image at a resolution of 50 cm/pixel. Our work, when viewed in the context of existing research, suggests that following sequence of events for the landscape evolution of the central Tharsis region: (1) the creation of a plateau region along the eastern margin of the Tharsis rise by east-directed, crustal-scale thrusting, (2) the coeval formation of a volcanic plateau that acted as the source of east-flowing lavas that filled a basin between the tectonically induced plateau in the east and the volcanically generated plateau, (3) continued east-west crustal shortening during the emplacement of the lava flows favored the formation of wrinkle ridges due to thermal weakening of the uppermost crust, (4) regional glaciation postdating lava emplacement produced extensive boulder-bearing materials, striated surfaces, and glacial eskers that are superposed on top of the earlier formed wrinkle ridges, and (5) deposition of locally highly concentrated glacial flours during deglaciation laid down selectively mantled the tectonically deformed and glacially modified landscape. Our work supports the early suggestion that the Tharsis wrinkle ridges were created by horizontal shortening induced by crustal-scale tectonic processes. However, the occurrence of flow-front-like margins of many mapped wrinkle ridges suggests that the deformation was ductile, at least locally, mostly like when the uppermost crust was still hot and weak. Glacial modification of the earlier formed wrinkle ridges means that the present-day wrinkle-ridge morphologies should not be used to invert the geometry of the blind thrust systems below the ridges.

Acknowledgements. We thank NASA for making the CTX and HiRISE images available and the HiRISE Team at the University of Arizona for providing the HiView software for analyzing the HiRISE images. We also thank the European Space Agency for making their HRSC DEM data available for this study. This research could never been conducted with the freely available JMARS sofreware, which is capable of doing everything demanded by this research. Feedback on the work from UCLA colleagues Dave Paige, Mackenzie Day, and Seulgi Moon helped improved the original manuscript. Finally, we thank that journal reviewers for their critical, thoughtful, detailed, and constructive comments. The work presented in this paper is a result of curiosity-driven research that was not supported by any funding agencies.

References

Allemand, P., & Thomas, P. G. (1995). Localization of Martian ridges by impact craters: Mechanical and chronological implications. Journal of Geophysical Research: Planets, 100(E2), 3251-3262.

Anderson, R. C., Dohm, J. M., Golombek, M. P., Haldemann, A. F., Franklin, B. J., Tanaka, K. L., ... & Peer, B. (2001). Primary centers and secondary concentrations of tectonic activity through time in the western hemisphere of Mars. Journal of Geophysical Research: Planets, 106(E9), 20563-20585.

Andrews-Hanna, J. C. (2020). The tectonic architecture of wrinkle ridges on Mars. Icarus, 351, 113937.

Ansan, V., & Mangold, N. (2006). New observations of Warrego Valles, Mars: Evidence for precipitation and surface runoff. Planetary and Space Science, 54(3), 219-242.

Ansan, V., & Mangold, N. (2013). 3D morphometry of valley networks on Mars from HRSC/MEX DEMs: Implications for climatic evolution through time. Journal of Geophysical Research: Planets, 118(9), 1873-1894.

Agard, P., Omrani, J., Jolivet, L., Whitechurch, H., Vrielynck, B., Spakman, W., ... & Wortel, R. (2011). Zagros orogeny: a subduction-dominated process. Geological Magazine, 148(5-6), 692-725.

Atkins, C. B. (2013). Geomorphological evidence of cold-based glacier activity in South Victoria Land, Antarctica. Geological Society, London, Special Publications, 381(1), 299-318.

Baker, V. R., Maruyama, S., & Dohm, J. M. (2007). Tharsis superplume and the geological evolution of early Mars. In Superplumes: Beyond plate tectonics (pp. 507-522). Springer, Dordrecht.

Baldwin, R. B. (1968). Lunar mascons: Another interpretation. Science, 162(3860), 1407-1408.

Bally, A. W., Gordy, P. L., & Stewart, G. A. (1966). Structure, Seismic Data, and Orogenic Evolution of Southern Canadian Rocky Mountains. Bulletin of Canadian Petroleum Geology, 14(3), 337-381.

Banerdt, W. B., Golombek, M. P., & Tanaka, K. L. (1992). Stress and tectonics on Mars. Mars, 249-297.

Baptista, A. R., Mangold, N., Ansan, V., Baratoux, D., Lognonné, P., Alves, E. I., ... & Neukum, G. (2008). A swarm of small shield volcanoes on Syria Planum, Mars. Journal of Geophysical Research: Planets, 113(E9).

Basilevsky, A. T., & Head, J. W. (2006). Impact craters on regional plains on Venus: Age relations with wrinkle ridges and implications for the geological evolution of Venus. Journal of Geophysical Research: Planets, 111(E3).

Benn, D. I., Bolch, T., Hands, K., Gulley, J., Luckman, A., Nicholson, L. I., ... & Wiseman, S. (2012). Response of debris-covered glaciers in the Mount Everest region to recent warming, and implications for outburst flood hazards. Earth-Science Reviews, 114(1-2), 156-174.

Berman, D. C., Balme, M. R., Rafkin, S. C., & Zimbelman, J. R. (2011). Transverse aeolian ridges (TARs) on Mars II: distributions, orientations, and ages. Icarus, 213(1), 116-130.

Bethell, E. M., Ernst, R. E., & Samson, C. (2022). Analysis of Venusian Wrinkle Ridge Morphometry Using Stereo-Derived Topography: A Case Study from Southern Eistla Regio. Journal of Geophysical Research: Planets, 127(5), e2021JE006879.

Bilotti, F., & Suppe, J. (1999). The global distribution of wrinkle ridges on Venus. Icarus, 139(1), 137-157.

Bouley, S., Baratoux, D., Paulien, N., Missenard, Y., & Saint-Bézar, B. (2018). The revised tectonic history of Tharsis. Earth and Planetary Science Letters, 488, 126-133.

Boulton, G. S. (1978). Boulder shapes and grain-size distributions of debris as indicators of transport paths through a glacier and till genesis. Sedimentology, 25(6), 773-799.

Bridges, N. T., Banks, M. E., Beyer, R. A., Chuang, F. C., Dobrea, E. N., Herkenhoff, K. E., ... & Wray, J. J. (2010). Aeolian bedforms, yardangs, and indurated surfaces in the Tharsis Montes as seen by the HiRISE Camera: Evidence for dust aggregates. Icarus, 205(1), 165-182.

Brunetti, M. T., Guzzetti, F., Cardinali, M., Fiorucci, F., Santangelo, M., Mancinelli, P., ... & Borselli, L. (2014). Analysis of a new geomorphological inventory of landslides in Valles Marineris, Mars. Earth and Planetary Science Letters, 405, 156-168.

Butcher, F. E., Balme, M. R., Conway, S. J., Gallagher, C., Arnold, N. S., Storrar, R. D., Lewis, S. R., Hagermann, A., & Davis, J. M. (2021). Sinuous ridges in Chukhung crater, Tempe Terra, Mars: Implications for fluvial, glacial, and glaciofluvial activity. Icarus, 357, 114131. https://doi.org/10.1016/j.icarus.2020.114131.

Bryan, W. B. (1973). Wrinkle-ridges as deformed surface crust on ponded mare lava. Lunar and Planetary Science Conference Proceedings, 4, 93-106.

Byrne, P. K., Klimczak, C., Celâl Şengör, A. M., Solomon, S. C., Watters, T. R., Hauck, I. I., & Steven, A. (2014). Mercury's global contraction much greater than earlier estimates. Nature Geoscience, 7(4), 301-307.

Byrne, P. K., Ghail, R. C., Şengör, A. C., James, P. B., Klimczak, C., & Solomon, S. C. (2021). A globally fragmented and mobile lithosphere on Venus. Proceedings of the National Academy of Sciences, 118(26), e2025919118.

Carr, M. H. (1973). Volcanism on mars. Journal of Geophysical Research, 78(20), 4049-4062.

Carr, M. H. (1974). Tectonism and volcanism of the Tharsis region of Mars. Journal of Geophysical Research, 79(26), 3943-3949.

Carr, M. H., & Head III, J. W. (2010). Geologic history of Mars. Earth and Planetary Science Letters, 294(3-4), 185-203.

Carr, M. H., Greeley, R., Blasius, K. R., Guest, J. E., & Murray, J. B. (1977). Some Martian volcanic features as viewed from the Viking orbiters. Journal of Geophysical Research, 82(28), 3985-4015.

Cassanelli, J. P., & Head, J. W. (2019). Glaciovolcanism in the Tharsis volcanic province of Mars: Implications for regional geology and hydrology. Planetary. and Space Science, 169, 45-69. https://doi.org/10.1016/j.pss.2019.02.006.

Chen, H., & Yin, A. (2022). Impacts of thrusting, extensional faulting, and glaciation on cratering records of Pluto’s largest moon Charon: Implications for the evolution of Kuiper belt objects. Earth and Planetary Physics, 6(6), 495-521.

Christensen, P. R., Engle, E., Anwar, S., Dickenshied, S., Noss, D., Gorelick, N., & Weiss-Malik, M. (2009). JMARS-a planetary GIS. In AGU Fall Meeting Abstracts (Vol. 2009, pp. IN22A-06).

Clark, P. U., & Walder, J. S. (1994). Subglacial drainage, eskers, and deforming beds beneath the Laurentide and Eurasian ice sheets. Geological Society of America Bulletin, 106(2), 304-314.

Cole, H. M., & Andrews-Hanna, J. C. (2017). The anatomy of a wrinkle ridge revealed in the wall of Melas Chasma, Mars. Journal of Geophysical Research: Planets, 122(5), 889-900.

Crane, K. T., & Klimczak, C. (2019). Tectonic patterns of shortening landforms in Mercury's northern smooth plains. Icarus, 317, 66-80.

Dębniak, K., Mège, D., & Gurgurewicz, J. (2017). Geomorphology of Ius Chasma, Valles Marineris, Mars. Journal of Maps, 13(2), 260-269.

Dickson, J. L., Kerber, L. A., Fassett, C. I., & Ehlmann, B. L. (2018, March). A global, blended CTX mosaic of Mars with vectorized seam mapping: A new mosaicking pipeline using principles of non-destructive image editing. In Lunar and planetary science conference (Vol. 49, pp. 1-2).

Dohm, J. M., Baker, V. R., Maruyama, S., & Anderson, R. C. (2007). Traits and evolution of the Tharsis superplume, Mars. In Superplumes: Beyond plate tectonics (pp. 523-536). Springer, Dordrecht.

Dohm, J. M., Maruyama, S., Kido, M., & Baker, V. R. (2018). A possible anorthositic continent of early Mars and the role of planetary size for the inception of Earth-like life. Geoscience Frontiers, 9(4), 1085-1098.

Edgett, K. S. (1997). Aeolian dunes as evidence for explosive volcanism in the Tharsis region of Mars. Icarus, 130(1), 96-114.

Edwards, C. S., Nowicki, K. J., Christensen, P. R., Hill, J., Gorelick, N., & Murray, K. (2011). Mosaicking of global planetary image datasets: 1. Techniques and data processing for Thermal Emission Imaging System (THEMIS) multi-spectral data. Journal of Geophysical Research: Planets, 116(E10). https://doi.org/10.1029/2010JE003755.

Elger, T. G. (1895). The Moon: A full description and map of its principal physical features. G. Philip & son.

Evans, D.J.A., 2003. Glacial Landsystems. Hodder Arnold, London. 532 pp.

Fergason, R.L, Hare, T.M., Laura, J., 2018, HRSC and MOLA Blended Digital Elevation Model at 200 m v2, Astrogeology PDS Annex, U.S. Geological Survey, URL: http://bit.ly/HRSC_MOLA_Blend_v0.

Fielder, G. (1961). Structure of the Moon's surface, New York, Pergamon Press, 266 p.

Fielder, G. (1965). Lunar geology: Chester Springs, Pennsylvania, Dufour Editions Inc., 184 p.

Fielder, G., & Kiang, T. (1962). The segmental structure of wrinkle ridges and the lunar grid system. The Observatory, 82, 8-9.

Freed, A. M., Melosh, H. J., & Solomon, S. C. (2001). Tectonics of mascon loading: Resolution of the strike-slip faulting paradox. Journal of Geophysical Research: Planets, 106(E9), 20603-20620.

Fueten, F., Flahaut, J., Le Deit, L., Stesky, R., Hauber, E., & Gwinner, K. (2011). Interior layered deposits within a perched basin, southern Coprates Chasma, Mars: Evidence for their formation, alteration, and erosion. Journal of Geophysical Research: Planets, 116(E2).

Gallagher, C., & Balme, M. (2015). Eskers in a complete, wet-based glacial system in the Phlegra Montes region, Mars. Earth and Planetary Science Letters, 431, 96-109.

Golabek, G. J., Keller, T., Gerya, T. V., Zhu, G., Tackley, P. J., & Connolly, J. A. (2011). Origin of the Martian dichotomy and Tharsis from a giant impact causing massive magmatism. Icarus, 215(1), 346-357.

Golombek, M. P., Plescia, J. B., & Franklin, B. J. (1991). Faulting and folding in the formation of planetary wrinkle ridges. Planetary Science Conference Proceedings, 21, 679–693.

Golombek, M. P., Anderson, F. S., & Zuber, M. T. (2001). Martian wrinkle ridge topography: Evidence for subsurface faults from MOLA. Journal of Geophysical Research: Planets, 106(E10), 23811-23821.

Golombek, M. P., Phillips, R. J., Watters, T. R., & Schultz, R. A. (2010). Mars tectonics. Planetary Tectonics, 11, 183-232.

Gourronc, M., Bourgeois, O., Mège, D., Pochat, S., Bultel, B., Massé, M., Le Deit, L., Le Mouélic, S. & Mercier, D. (2014). One million cubic kilometers of fossil ice in Valles Marineris: Relicts of a 3.5 Gy old glacial landsystem along the Martian equator. Geomorphology, 204, 235-255.

Grant, J. A., Irwin III, R. P., Grotzinger, J. P., Milliken, R. E., Tornabene, L. L., McEwen, A. S., ... & Thomson, B. J. (2008). HiRISE imaging of impact megabreccia and sub-meter aqueous strata in Holden Crater, Mars. Geology, 36(3), 195-198.

Grau Galofre, A., Jellinek, A. M., & Osinski, G. R. (2020). Valley formation on early Mars by subglacial and fluvial erosion. Nature Geoscience, 13(10), 663-668.

Greeley, R., & Spudis, P. D. (1978a). Volcanism in the cratered terrain hemisphere of Mars. Geophysical Research Letters, 5(6), 453-455.

Greeley, R., & Spudis, P. D. (1978b). Ridges in Western Columbia Plateau, Washington-Analogs to Mare-Type Ridges?. In Lunar and Planetary Science Conference (Vol. 9, pp. 411-412).

Guest, J. E., & Fielder, G. (1968). Lunar ring structures and the nature of the maria. Planetary and Space Science, 16(5), 665-673.

Guest, J. E. (1971). Geology of the far side crater Tsiolkovsky, in Geology and Physics of the Moon, edited by G. Fielder, pp. 93-103, Elsevier, Amsterdam.

Hansen, V. L., & Olive, A. (2010). Artemis, Venus: The largest tectonomagmatic feature in the solar system?. Geology, 38(5), 467-470.

Harder, H., & Christensen, U. R. (1996). A one-plume model of Martian mantle convection. Nature, 380(6574), 507-509.

Hartmann, W. K., Anguita, J., Miguel, A., Berman, D. C., & Ryan, E. V. (2001). Martian cratering 7: The role of impact gardening. Icarus, 149(1), 37-53.

Hauber, E., Bleacher, J., Gwinner, K., Williams, D., & Greeley, R. (2009). The topography and morphology of low shields and associated landforms of plains volcanism in the Tharsis region of Mars. Journal of Volcanology and Geothermal Research, 185(1-2), 69-95.

Head III, J. W., Kreslavsky, M. A., & Pratt, S. (2002). Northern lowlands of Mars: Evidence for widespread volcanic flooding and tectonic deformation in the Hesperian Period. Journal of Geophysical Research: Planets, 107(E1), 3-1.

Head, J. W., Marchant, D. R., Dickson, J. L., Kress, A. M., & Baker, D. M. (2010). Northern mid-latitude glaciation in the Late Amazonian period of Mars: Criteria for the recognition of debris-covered glacier and valley glacier landsystem deposits. Earth and Planetary Science Letters, 294(3-4), 306-320.

Hicock, S. R. (1991). On subglacial stone pavements in till. The Journal of Geology, 99(4), 607-619.

Howard, K. A., & Muehlberger, W. R. (1973). Mare ridges and related studies: Part C: Lunar thrust faults in the Taurus-Littrow region,

Ivanov, M. A., & Head, J. W. (2011). Global geological map of Venus. Planetary and Space Science, 59(13), 1559-1600.

Li, B., Ling, Z., Zhang, J., Chen, J., Ni, Y., & Liu, C. (2018). Displacement-length ratios and contractional strains of lunar wrinkle ridges in Mare Serenitatis and Mare Tranquillitatis. Journal of Structural Geology, 109, 27-37.

Lucchitta, B. K. (1978). Morphology of chasma walls, Mars. J. Res. US Geol. Surv, 6(5), 651-662.

Lucchitta, B. K., & Klockenbrink, J. L. (1981). Ridges and scarps in the equatorial belt of Mars. The moon and the planets, 24(4), 415-429.

Karagoz, O., Kenkmann, T., & Wulf, G. (2022a). Insights into the subsurface structure of wrinkle ridges on Mars. Earth and Planetary Science Letters, 595, 117759.

Karagoz, O., Kenkmann, T., & Wulf, G. (2022b). Circum-Tharsis wrinkle ridges at Lunae Planum: Morphometry, formation, and crustal implications. Icarus, 374, 114808.

Kargel, J. S., & Strom, R. G. (1992). Ancient glaciation on Mars. Geology, 20(1), 3-7.

Kreslavsky, M. A., & Basilevsky, A. T. (1998). Morphometry of wrinkle ridges on Venus: Comparison with other planets. Journal of Geophysical Research: Planets, 103(E5), 11103-11111.

Lillis, R.J., Dufek, J., Bleacher, J.E., & Manga, M., 2009, Demagnetization of crust by magmatic intrusion near the Arsia Mons volcano: Magnetic and thermal implications for the development of the Tharsis province, Mars: Journal of Volcanology and Geothermal Research, v. 185, p. 123–138, doi:10.1016/j.jvolgeores.2008.12.007.

Malin, M. C., Bell, J. F., Cantor, B. A., Caplinger, M. A., Calvin, W. M., Clancy, R. T., Edgett, K. S., Edwards, L., Haberle, R. M., James, P. B., Lee, S. W., Ravine, M. A., Thomas, P. C., & Wolff, M. J. (2007). Context camera investigation on board the Mars Reconnaissance Orbiter. Journal of Geophysical Research: Planets, 112(E5). https://doi.org/10.1029/2006JE002808.

Mangold, N., Allemand, P., & Thomas, P. G. (1998). Wrinkle ridges of Mars: Structural analysis and evidence for shallow deformation controlled by ice-rich décollements. Planetary and Space Science, 46(4), 345-356.

Mangold, N., Ansan, V., Masson, P., Quantin, C., & Neukum, G. (2008). Geomorphic study of fluvial landforms on the northern Valles Marineris plateau, Mars. Journal of Geophysical Research: Planets, 113(E8).

Mangold, N., Loizeau, D., Poulet, F., Ansan, V., Baratoux, D., LeMouelic, S., Bardintzeff, J.M., Platevoet, B., Toplis, M., Pinet, P. & Masson, P. (2010). Mineralogy of recent volcanic plains in the Tharsis region, Mars, and implications for platy-ridged flow composition. Earth and Planetary Science Letters, 294(3-4), 440-450.

Maxwell, T. A., and Gifford, A. W. (1980). Ridge system of Caloris: Compari son with lunar basins, Proc. Lunar Planet. Sci. Conf, 11th, 2447-2462.

Maxwell, T. A., El-Baz, F., & Ward, S. H. (1975). Distribution, morphology, and origin of ridges and arches in Mare Serenitatis. Geological Society of America Bulletin, 86(9), 1273-1278.

Mège, D., & Bourgeois, O. (2011). Equatorial glaciations on Mars revealed by gravitational collapse of Valles Marineris wallslopes. Earth and Planetary Science Letters, 310(3-4), 182-191.

Mège, D., & Masson, P. (1996a). A plume tectonics model for the Tharsis province, Mars. Planetary and Space Science, 44(12), 1499-1546.

Mège, D., & Masson, P. (1996b). Stress models for Tharsis formation, Mars. Planetary and Space Science, 44(12), 1471-1497.

Mège, D., & Reidel, S. P. (2001). A method for estimating 2D wrinkle ridge strain from application of fault displacement scaling to the Yakima folds, Washington. Geophysical Research Letters, 28(18), 3545-3548.

McGill, G. E. (1993). Wrinkle ridges, stress domains, and kinematics of Venusian plains. Geophysical Research Letters, 20(21), 2407-2410.

McGill, G. E. (2004). Tectonic and stratigraphic implications of the relative ages of Venusian plains and wrinkle ridges. Icarus, 172(2), 603-612.

Montési, L. G., & Zuber, M. T. (2003). Clues to the lithospheric structure of Mars from wrinkle ridge sets and localization instability. Journal of Geophysical Research: Planets, 108(E6).

Mouginis-Mark, P. J. (1987). Water or ice in the Martian regolith?: Clues from rampart craters seen at very high resolution. Icarus, 71(2), 268-286.

Mouginis-Mark, P. J., & Wilson, L. (2019). Late-stage intrusive activity at Olympus Mons, Mars: Summit inflation and giant dike formation. Icarus, 319, 459-469.

Mouginis-Mark, P. J., Zimbelman, J. R., Crown, D. A., Wilson, L., & Gregg, T. K. (2022). Martian volcanism: Current state of knowledge and known unknowns. Geochemistry, 125886.

Mueller, K., & Golombek, M. (2004). Compressional structures on Mars. Annu. Rev. Earth Planet. Sci., 32, 435-464.

Murchie, S. L., Watters, T. R., Robinson, M. S., Head, J. W., Strom, R. G., Chapman, C. R., ... & Blewett, D. T. (2008). Geology of the Caloris basin, Mercury: A view from MESSENGER. Science, 321(5885), 73-76.

Murray, B. C., Belton, M. J., Danielson, G. E., Davies, M. E., Gault, D., Hapke, B., ... & Trask, N. (1974). Mariner 10 pictures of Mercury: First results. Science, 184(4135), 459-461.

Nahm, A. L., & Schultz, R. A. (2011). Magnitude of global contraction on Mars from analysis of surface faults: Implications for martian thermal history. Icarus, 211(1), 389-400.

Neukum, G., Jaumann, R., Hoffmann, H., Hauber, E., Head, J. W., Basilevsky, A. T., Ivanov, B. A., Werner, S. C., van Gasselt, S., Murray, J. B., & McCord, T. (2004). Recent and episodic volcanic and glacial activity on Mars revealed by the High Resolution Stereo Camera. Nature, 432(7020), 971-979. https://doi.org/10.1038/nature03231.

Okubo, C. H., & Schultz, R. A. (2004). Mechanical stratigraphy in the western equatorial region of Mars based on thrust fault–related fold topography and implications for near-surface volatile reservoirs. Geological Society of America Bulletin, 116(5-6), 594-605.

Parsons, W.H. (1969) Criteria for the recognition of volcanic breccia. Geological Society of America Memoir, 115, 263-304.

Phillips, R. J., & Lambeck, K. (1980). Gravity fields of the terrestrial planets: Long-wavelength anomalies and tectonics. Reviews of Geophysics, 18(1), 27-76.

Phillips, R. J., Zuber, M. T., Solomon, S. C., Golombek, M. P., Jakosky, B. M., Banerdt, W. B., ... & Hauck II, S. A. (2001). Ancient geodynamics and global-scale hydrology on Mars. Science, 291(5513), 2587-2591.

Plescia, J. B., & Golombek, M. P. (1986). Origin of planetary wrinkle ridges based on the study of terrestrial analogs. Geological Society of America Bulletin, 97(11), 1289-1299.

Price, R. (1981). The Cordilleran foreland thrust and fold belt in the southern Canadian Rocky Mountains. Geological Society, London, Special Publications, 9(1), 427-448.

Rahn, P. H. (1971). Lunar Wrinkle Ridges Indicative of Strike-Slip Faulting: Discussion. Geological Society of America Bulletin, 82(8), 2365-2366.

Reese, C. C., Solomatov, V. S., Baumgardner, J. R., Stegman, D. R., & Vezolainen, A. V. (2004). Magmatic evolution of impact-induced Martian mantle plumes and the origin of Tharsis. Journal of Geophysical Research: Planets, 109(E8).

Reidel, S. P. (1984). The Saddle Mountains; the evolution of an anticline in the Yakima fold belt. American Journal of Science, 284(8), 942-978.

Richardson, J. A., Bleacher, J. E., & Glaze, L. S. (2013). The volcanic history of Syria Planum, Mars. Journal of Volcanology and Geothermal Research, 252, 1-13.

Richardson, J. A., Bleacher, J. E., Connor, C. B., & Glaze, L. S. (2021). Small Volcanic Vents of the Tharsis Volcanic Province, Mars. Journal of Geophysical Research: Planets, 126(2), e2020JE006620.

Ruj, T., & Kawai, K. (2021). A global investigation of wrinkle ridge formation events; implications towards the thermal evolution of Mars. Icarus, 369, 114625.

Schleicher, L. S., Watters, T. R., Martin, A. J., & Banks, M. E. (2019). Wrinkle ridges on Mercury and the Moon within and outside of Mascons. Icarus, 331, 226-237.

Schubert, G., Solomon, S.C., Turcotte, D.L., Drake, M.J., Sleep, N.H., 1992. Origin and thermal evolution of Mars. In: Kieffer, H.H., Jakosky, B.M., Snyder, C.M., Matthews, M.S. (Eds.), Mars. Univ. of Arizona Press, Tucson, pp. 147–183

Schultz, R. A. (2000). Localization of bedding plane slip and backthrust faults above blind thrust faults: Keys to wrinkle ridge structure. Journal of Geophysical Research: Planets, 105(E5), 12035-12052.

Scott, E., & Wilson, L. (2003). Did the Alba Patera and Syria Planum regions of Mars lose their lithospheric roots in convective overturn events?. Journal of Geophysical Research: Planets, 108(E5).

Shreve, R. L. (1985). Esker characteristics in terms of glacier physics, Katahdin esker system, Maine. Geological Society of America Bulletin, 96(5), 639-646.

Sleep, N. H. (1994). Martian plate tectonics. Journal of Geophysical Research: Planets, 99(E3), 5639-5655.

Smellie, J. L., Rocchi, S., & Armienti, P. (2011). Late Miocene volcanic sequences in northern Victoria Land, Antarctica: products of glaciovolcanic eruptions under different thermal regimes. Bulletin of Volcanology, 73(1), 1-25.

Smith, D. E., Zuber, M. T., Solomon, S. C., Phillips, R. J., Head, J. W., Garvin, J. B., ... & Duxbury, T. C. (1999). The global topography of Mars and implications for surface evolution. Science, 284(5419), 1495-1503.

Solomon, S. C., & Head, J. W. (1979). Vertical movement in mare basins: Relation to mare emplacement, basin tectonics, and lunar thermal history. Journal of Geophysical Research: Solid Earth, 84(B4), 1667-1682.

Solomon, S. C., & Head, J. W. (1980). Lunar mascon basins: Lava filling, tectonics, and evolution of the lithosphere. Reviews of Geophysics, 18(1), 107-141.

Solomon, S. C., & Head, J. W. (1982). Evolution of the Tharsis province of Mars: The importance of heterogeneous lithospheric thickness and volcanic construction. Journal of Geophysical Research: Solid Earth, 87(B12), 9755-9774.

Solomon, S. C., Aharonson, O., Aurnou, J. M., Banerdt, W. B., Carr, M. H., Dombard, A. J., Frey, H.V., Golombek, M.P., Hauck, S.A., Head, J.W. & Jakosky, B. M. (2005). New perspectives on ancient Mars. Science, 307(5713), 1214-1220.

Stevenson, D. J. (2001). Mars' core and magnetism. Nature, 412(6843), 214-219.

Strom, R. G. (1972). Lunar mare ridges, rings and volcanic ring complexes, in Runcorn, S. K., and Urey, H. C., eds., The Moon, IAU Symposium no. 47, p. 187-215.

Strom, R.G. (1979) Mercury: A post-Mariner 10 assessment: Space Science Reviews, v. 24, p. 3-70.

Strom, R. G., Murray, B. C., Belton, M. J., Danielson, G. E., Davies, M. E., Gault, D. E., ... & Klaasen, K. (1975). Preliminary imaging results from the second Mercury encounter. Journal of Geophysical Research, 80(17), 2345-2356.

Suppe, J. (1983). Geometry and kinematics of fault-bend folding. American Journal of science, 283(7), 684-721.

Tanaka, K. L., Golombek, M. P., & Banerdt, W. B. (1991). Reconciliation of stress and structural histories of the Tharsis region of Mars. Journal of Geophysical Research: Planets, 96(E1), 15617-15633.

Tanaka, K. L., Skinner Jr, J. A., Dohm, J. M., Irwin III, R. P., Kolb, E. J., Fortezzo, C. M., Platz, T., Michael, G. G., & Hare, T. M. (2014). Geologic map of Mars. http://dx.doi.org/10.3133/sim3292

Tjia, H. D. (1970). Lunar wrinkle ridges indicative of strike-slip faulting. Geological Society of America Bulletin, 81(10), 3095-3100.

Tornabene, L. L., Osinski, G. R., McEwen, A. S., Wray, J. J., Craig, M. A., Sapers, H. M., & Christensen, P. R. (2013). An impact origin for hydrated silicates on Mars: A synthesis. Journal of Geophysical Research: Planets, 118(5), 994-1012.

Ward, A. W., Doyle, K. B., Helm, P. J., Weisman, M. K., & Witbeck, N. E. (1985). Global map of eolian features on Mars. Journal of Geophysical Research: Solid Earth, 90(B2), 2038-2056.

Warner, N. H., Golombek, M. P., Sweeney, J., Fergason, R., Kirk, R., & Schwartz, C. (2017). Near surface stratigraphy and regolith production in southwestern Elysium Planitia, Mars: implications for Hesperian-Amazonian terrains and the InSight lander mission. Space Science Reviews, 211(1), 147-190.

Warren, W. P., & Ashley, G. M. (1994). Origins of the ice-contact stratified ridges (eskers) of Ireland. Journal of Sedimentary Research, 64(3a), 433-449.

Watters, T. R. (1988). Wrinkle ridge assemblages on the terrestrial planets. Journal of Geophysical Research: Solid Earth, 93(B9), 10236-10254.

Watters, T. R. (1991). Origin of periodically spaced wrinkle ridges on the Tharsis Plateau of Mars. Journal of Geophysical Research: Planets, 96(E1), 15599-15616.

Watters, T. R. (1992). System of tectonic features common to Earth, Mars, and Venus. Geology, 20(7), 609-612.

Watters, T. R. (1993). Compressional tectonism on Mars. Journal of Geophysical Research: Planets, 98(E9), 17049-17060.

Watters, T. R. (2004). Elastic dislocation modeling of wrinkle ridges on Mars. Icarus, 171(2), 284-294.

Watters, T. R. (2021). A case for limited global contraction of Mercury. Nature Communications Earth & Environment, 2(1), 1-9.

Watters, T. R. (2022). Lunar Wrinkle Ridges and the Evolution of the Nearside Lithosphere. Journal of Geophysical Research: Planets, 127(3), e2021JE007058.

Watters, T. R., & Robinson, M. S. (1997). Radar and photoclinometric studies of wrinkle ridges on Mars. Journal of Geophysical Research: Planets, 102(E5), 10889-10903.

Watters, T. R., Head, J. W., Solomon, S. C., Robinson, M. S., Chapman, C. R., Denevi, B. W., ... & Strom, R. G. (2009a). Evolution of the Rembrandt impact basin on Mercury. Science, 324(5927), 618-621.

Watters, T. R., Murchie, S. L., Robinson, M. S., Solomon, S. C., Denevi, B. W., André, S. L., & Head, J. W. (2009b). Emplacement and tectonic deformation of smooth plains in the Caloris basin, Mercury. Earth and Planetary Science Letters, 285(3-4), 309-319.

Weiss, D. K., & Head, J. W. (2014). Ejecta mobility of layered ejecta craters on Mars: Assessing the influence of snow and ice deposits. Icarus, 233, 131-146.

Wilhelms, D. E. (1974). Comparison of Martian and lunar geologic provinces. Journal of Geophysical Research, 79(26), 3933-3941.

Williams, R. M., Irwin III, R. P., & Zimbelman, J. R. (2009). Evaluation of paleohydrologic models for terrestrial inverted channels: Implications for application to martian sinuous ridges. Geomorphology, 107(3-4), 300-315.

Wise, D. U., Golombek, M. P., & McGill, G. E. (1979). Tectonic evolution of Mars. Journal of Geophysical Research: Solid Earth, 84(B14), 7934-7939.

Yin, A. (2012a). Structural analysis of the Valles Marineris fault zone: Possible evidence for large-scale strike-slip faulting on Mars. Lithosphere, 4(4), 286-330. https://doi.org/10.1130/L192.1

Yin, A. (2012b). An episodic slab-rollback model for the origin of the Tharsis rise on Mars: Implications for initiation of local plate subduction and final unification of a kinematically linked global plate-tectonic network on Earth. Lithosphere, 4(6), 553-593. https://doi.org/10.1130/L195.1

Yin, A. (2006). Cenozoic tectonic evolution of the Himalayan orogen as constrained by along-strike variation of structural geometry, exhumation history, and foreland sedimentation. Earth-Science Reviews, 76(1-2), 1-131.

Yin, A., Moon, S., & Day, M. (2021). Landform evolution of Oudemans crater and its bounding plateau plains on Mars: Geomorphological constraints on the Tharsis ice-cap hypothesis. Icarus, 360, 114332. https://doi.org/10.1016/j.icarus.2021.114332

Yue, Z., Li, W., Di, K., Liu, Z., & Liu, J. (2015). Global mapping and analysis of lunar wrinkle ridges. Journal of Geophysical Research: Planets, 120(5), 978-994.

Yue, Z., Michael, G. G., Di, K., & Liu, J. (2017). Global survey of lunar wrinkle ridge formation times. Earth and Planetary Science Letters, 477, 14-20.

Zaki, A. S., Pain, C. F., Edgett, K. S., & Giegengack, R. (2018). Inverted stream channels in the Western Desert of Egypt: Synergistic remote, field observations and laboratory analysis on Earth with applications to Mars. Icarus, 309, 105-124.

Zhong, S. (2009). Migration of Tharsis volcanism on Mars caused by differential rotation of the lithosphere. Nature Geoscience, 2(1), 19-23. https://doi.org/10.1038/ngeo392.

Zuber, M. T. (1995). Wrinkle ridges, reverse faulting, and the depth penetration of lithospheric strain in Lunae Planum, Mars. Icarus, 114(1), 80-92.

Zuber, M.T., 2001. The crust and mantle of Mars. Nature 412 (6843), 220–227.

Zuber, M. T., & Aist, L. L. (1990). The shallow structure of the Martian lithosphere in the vicinity of the ridged plains. Journal of Geophysical Research: Solid Earth, 95(B9), 14215-14230.

Figure Captions

Figure 1. (A)-(I) Competing models for wrinkle-ridge formation. See text for details.

Figure 2. (A) A Google MarsTM image of the Tharsis rise of Mars. The image also shows the geographic locations of Sinai Planum, Valles Marineris, Thaumasia Planum, Coracis Fossae, Solis Planum, and Syria Planum. (B) A DEM map of Solis Dorsa and its surrounding areas. Also shown in this image are locations of Figs. 3A-3C. (C) A black and white map of nighttime temperatures that is blended with a THEMIS image, a CTX image, and a shaded DEM relief map. Darker-toned areas indicate higher nighttime temperatures. Numbers are geologic features described in the text, and yellow lines outline the extent of viscous-flow ejecta deposits of rampart-type impact craters marked as RC. Craters without well-defined impact ejecta apron and rim ridges occur in the highest-elevation area of Thaumasia Planum, which are marked as NR for non-rampart-type impact craters. The white box marks the location of Fig. 4A.

Figure 3. (A)-(C) are colored nighttime temperature maps that are blended with a THEMIS image, a CTX image, and a shaded DEM relief map. Brighter-colored areas indicate higher nighttime temperatures. Numbers refer to landform features described in the text. See Fig. 2 for the locations of the three panels.

Figure 4. (A) A colored nighttime temperature map that is blended with a THEMIS image, a CTX image, and a shaded DEM relief map. Numbers on the image mark the locations of the geomorphological features mentioned in the text. White straight line AB marks the topographic profile shown in (C). (B) A DEM map of the same area as shown in (A), with blue arrows pointing to wrinkle ridges and white arrows pointing to the east-trending, lower-relief ridges marked by

darker- and lighter-toned bands in the nighttime temperature map. The ridges are interpreted as lava flows (see text for details). Letters AB marks the location of the topographic profile shown in (C). (C) Topographic profile along line across east-trending ridges. See (C) for location.

Figure 5. (A) DEM map of the Solis Dorsa wrinkle ridge field and locations of profiles 1 and 2 shown in (B) and (C). Also shown is the location of Fig. 6A. (B) Topographic profile across the whole Solis Dorsa wrinkle ridge field. Yellow arrows indicate the locations of wrinkle ridges in the cross section. (C) Topographic profile across the study area in the southern part of the Solis Dorsa wrinkle ridge field.

Figure 6. (A) A black-and-white nighttime-temperature map that is blended with a THEMIS image, a CTX image, and a DEM shaded relief map. Numbers next to the white boxes are referred to as investigation sites in this study, which correspond to the locations of the analyzed HiRISE images with their identification numbers indicated on the side of the image. (B) Geomorphological map of the same area as shown in (B). See map legends and text for the description of the mapped units.

Figure 7. (A) A CTX image that shows a wrinkle ridge cutting across an impact crater. (B) A CTX image that shows an impact crater terminating a wrinkle ridge. See Fig. 6A for the locations of the two images and the text for details.

Figure 8. Zoom-in HiRISE images (A-K) that show boulder-bearing surfaces and/or striated surfaces on top of the mapped wrinkle ridges. The site number and the HiRISE identification number are indicated on each image, which correspond to those listed in Fig. 6. See text for details.

Figure 9. HiRISE images (A-D) that shows boulder-bearing surfaces, light-toned eolian bed forms, and breached crater rim ridges exposed on the inter-ridge plains. The site number and the HiRISE identification number are indicated on each image, which correspond to those listed in Fig. 6. See text for details.

Figure 10. HiRISE images of craters mapped in Fig. 6. (A) An overall view of the images shown in (B) and (C). (B) A viscous-flow-like feature that is a part of the impact ejecta blanket of a rampart crater. (C) Bedding exposed on a crater wall. (D) An overall view of the image shown in (E) and (F). (E) Viscous-flow-like features as a part of the impact ejecta blanket from a rampart crater. (F) Impact ejecta rays from a crater. Also shown is bedding on a crater wall. (G) Bedding exposed on a crater wall. (H) A close-up view of weathering-resistant beds on a crater wall. Also shown is a lobate ridge on the crater floor.

Figure 11. HiRISE images that show lobate-apron-like landforms with lava-flow-front-like margins. Also shown are a tongue-shaped sheet in (A) and lobate ridges in (B) and (C). The site number and the HiRISE identification number are indicated on each image, which correspond to those listed in Fig. 6. (D)-(F) show interpreted outlines of the key geomorphological features shown in (A)-(C).

Figure 12. HiRISE images of sinuous, sharp-crested, boulder-bearing ridges on top of a wrinkle ridge. The site number and the HiRISE identification number are indicated on the image, which correspond to the same number shown in Fig. 6. (A) Sinuous, sharp-crested, boulder-bearing ridges and ridge networks are top of a flat wrinkle ridge. Also shown is the location of (B). (B) A close-up view of boulder-bearing ridges and the location of (C). (C) A zoom-in view of the same boulder-bearing ridge as shown in (B) and location of (D). (D) Meter-sized boulders defining inclined layers exposed on the ridge side.

Figure 13. (A) HiRISE image (site 11 and ESP_018071_1540) at a resolution of 50 cm/pixel. White boxes indicate the locations of Figs. 14A, 15A, 16A, and 17A. (B) Geomorphological map interpreted from image (A). See text for details.

Figure 14. (A) An overview image (site 11 and HiRISE image ESP_018071_1540) of the northern plains. White boxes indicate locations of (B), (C), (E), (F), and (G), and S1 to S4 mark the mapped scarps shown in Fig. 13B. Images (B)-(G) display geomorphological features described in the text.

Figure 15. (A) An overview image (site 11 and HiRISE image ESP_018071_1540) of the southern plains. White boxes indicate the locations of (B), (D), (H), and (K). Images (B)-(K) show geomorphological features described in the text.

Figure 16. Zoom-in views from HiRISE image ESP_018071_1540, which show geomorphological features in the southern foothill terrain and the southern plains unit described in the text. Panel (A) provides the locations of other panels shown in this figure.

Figure 17. Striations, scarps, and scarp-truncated craters. See text for details.

Figure 18. Competing models on the origin of surficial meter-scale boulders across the study area shown in Fig. 6: (A) impact gardening model, (B) autobrecciation model, and (C) debris-covered glacier.

Figure 19. A basement-subduction model for the development of the thin-skinned fold belt represented by the wrinkle ridge field in Solis Dorsa. (A) Emplacement of lava flows coeval with crustal shortening. (B) Ductile folding of warm lava beds in Solis Dorsa. (C) Pre-volcanism basement is subducted below the ductile root of the volcanic center during the thin-skinned folding of supracrustal lava beds. The upwelling of the hot and ductile lava beds created the flow-front-like morphology of some of the wrinkle ridge margins.

Figure 20. Landscape evolution model of the central and eastern Tharsis rise. (A) Formation of the Thaumasia Planum highlands by thrusting and the coeval development of the Syria volcanic plateau. (B) Continued coeval development of the Syria volcanic plateau and the rise of the Thaumasia Planum highlands. (C) Synchronous folding and eastward emplacement of volcanic flows that filled the Solis Dorsa basin. (D) Emplacement of an ice sheet over the volcanic pile in Solis Dorsa. (E) Deglaciation and deposition of locally concentrated glacial flours that created mantled terrains.

Figure 1

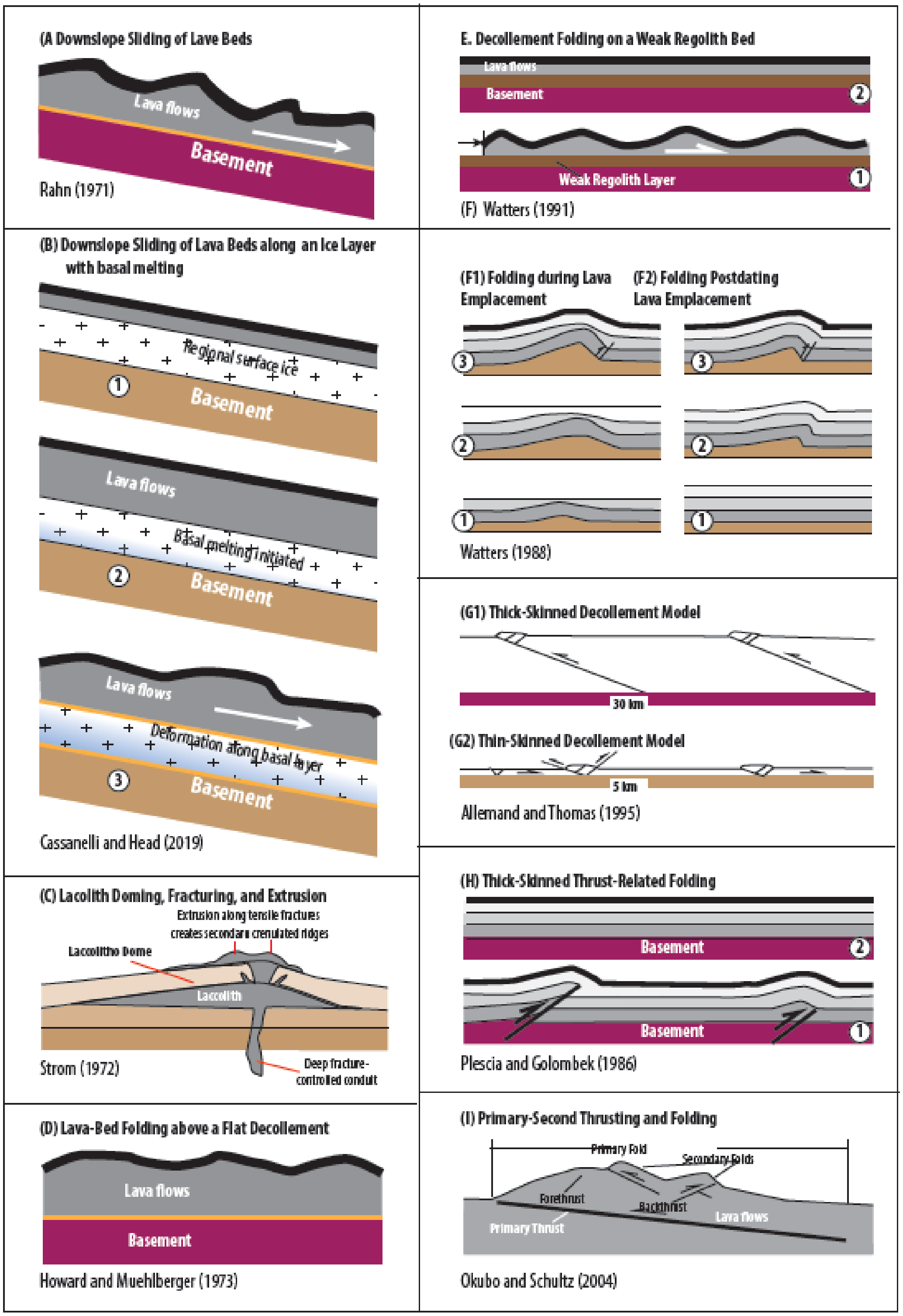
(A Downslope Sliding of Lave Beds
Lava flows
Basement
Rahn (1971)
E. Decollement Folding on a Weak Regolith Bed
Lava flows
Basement
2
Weak Regolith Layer
1
(F) Watters (1991)
(B) Downslope Sliding of Lava Beds along an Ice Layer with basal melting
Regional surface ice
1
Basement
Lava flows
Basal melting initiated
2
Basement
Lava flows
Deformation along basal layer
3
Basement
Cassanelli and Head (2019)
(F1) Folding during Lava Emplacement
(F2) Folding Postdating Lava Emplacement
3
3
2
2
1
1
Watters (1988)
(G1) Thick-Skinned Decollement Model
30 km
(G2) Thin-Skinned Decollement Model
5 km
Allemand and Thomas (1995)
(C) Lacolith Doming, Fracturing, and Extrusion
Extrusion along tensile fractures
Lacolith
Strom (1972)
Deep fracture-controlled conduit
(H) Thick-Skinned Thrust-Related Folding
Basement
2
Basement
1
Plescia and Golombek (1986)
(D) Lava-Bed Folding above a Flat Decollement
Lava flows
Basement
Howard and Muehlberger (1973)
(I) Primary-Second Thrusting and Folding
Primary Fold
Secondary Folds
Forethrust
Backthrust
Primary Thrust
Lava flows
Okubo and Schultz (2004)

Figure 2

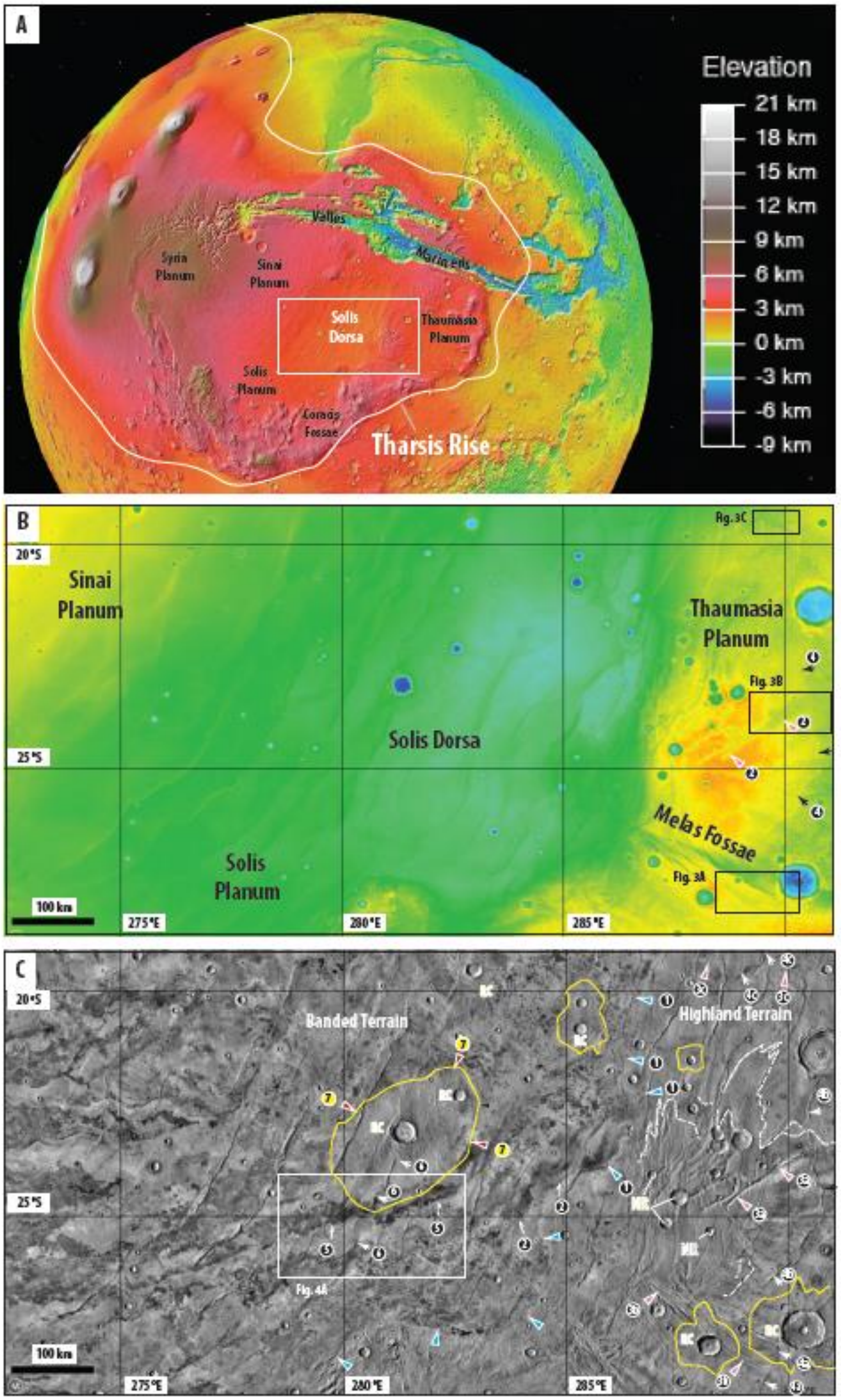
A
Elevation
21 km
18 km
15 km
12 km
9 km
6 km
3 km
0 km
-3 km
-6 km
-9 km
Valles
Marineris
Syria
Planum
Sinai
Planum
Solis
Dorsa
Thaumasia
Planum
Solis
Planum
Coracis
Fossae
Tharsis Rise
B
Fig. 3C
20°S
Sinai
Planum
Thaumasia
Planum
Fig. 3B
Solis Dorsa
25°S
Melas Fossae
Fig. 3A
Solis
Planum
100 km
275°E
280°E
285°E
C
20°S
Banded Terrain
Highland Terrain
25°S
Fig. 4A
100 km
275°E
280°E
285°E

Figure 3

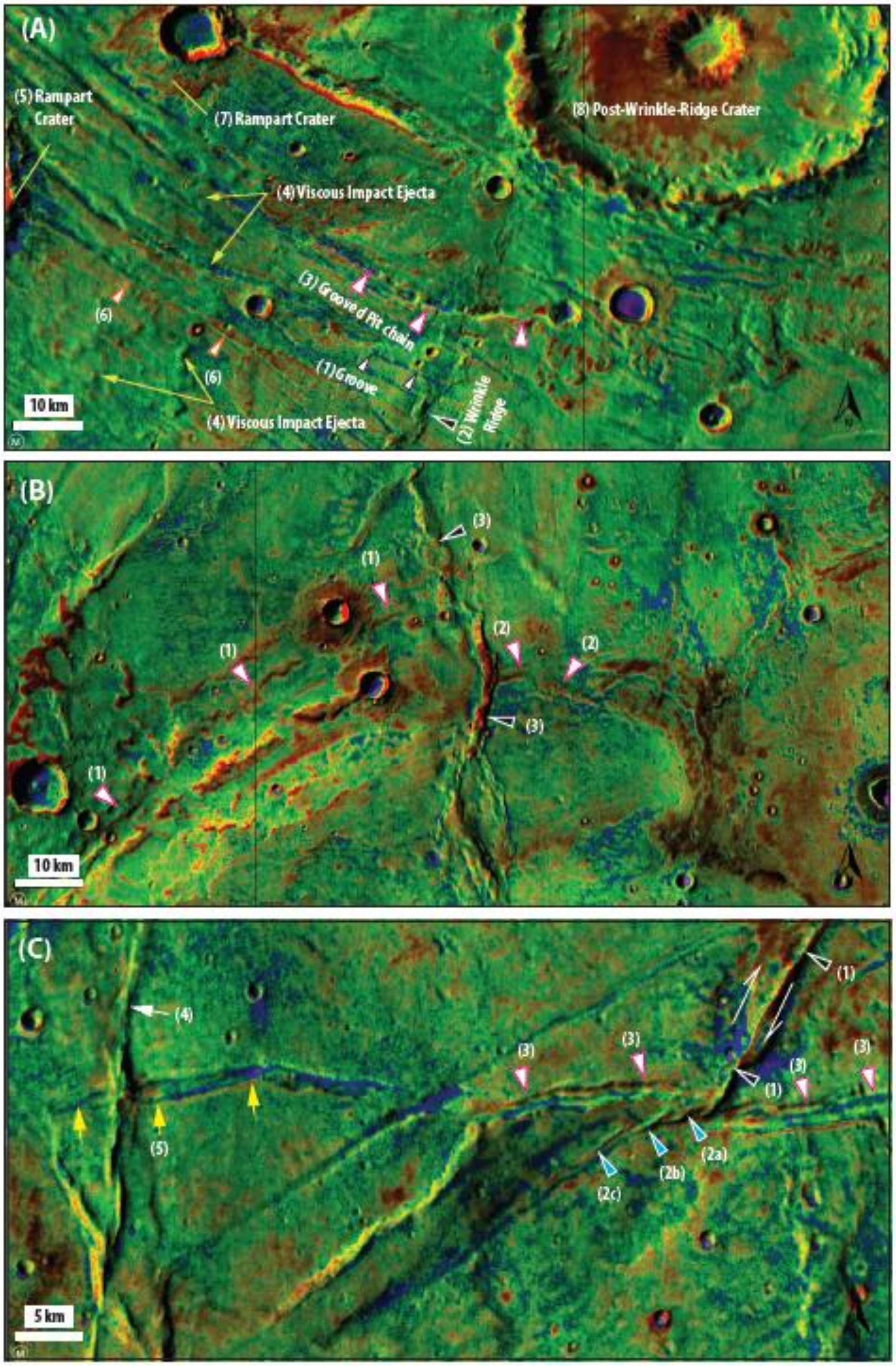

(A)
(5) Rampart Crater
(7) Rampart Crater
(8) Post-Wrinkle-Ridge Crater
(4) Viscous Impact Ejecta
(3) Grooved Pit chain
(6)
(1) Groove
(6)
(4) Viscous Impact Ejecta
(2) Wrinkle Ridge
10 km
(B)
(3)
(1)
(2)
(2)
(1)
(3)
(1)
10 km
(C)
(4)
(1)
(3)
(3)
(3)
(3)
(1)
(5)
(2a)
(2b)
(2c)
5 km

Figure 4

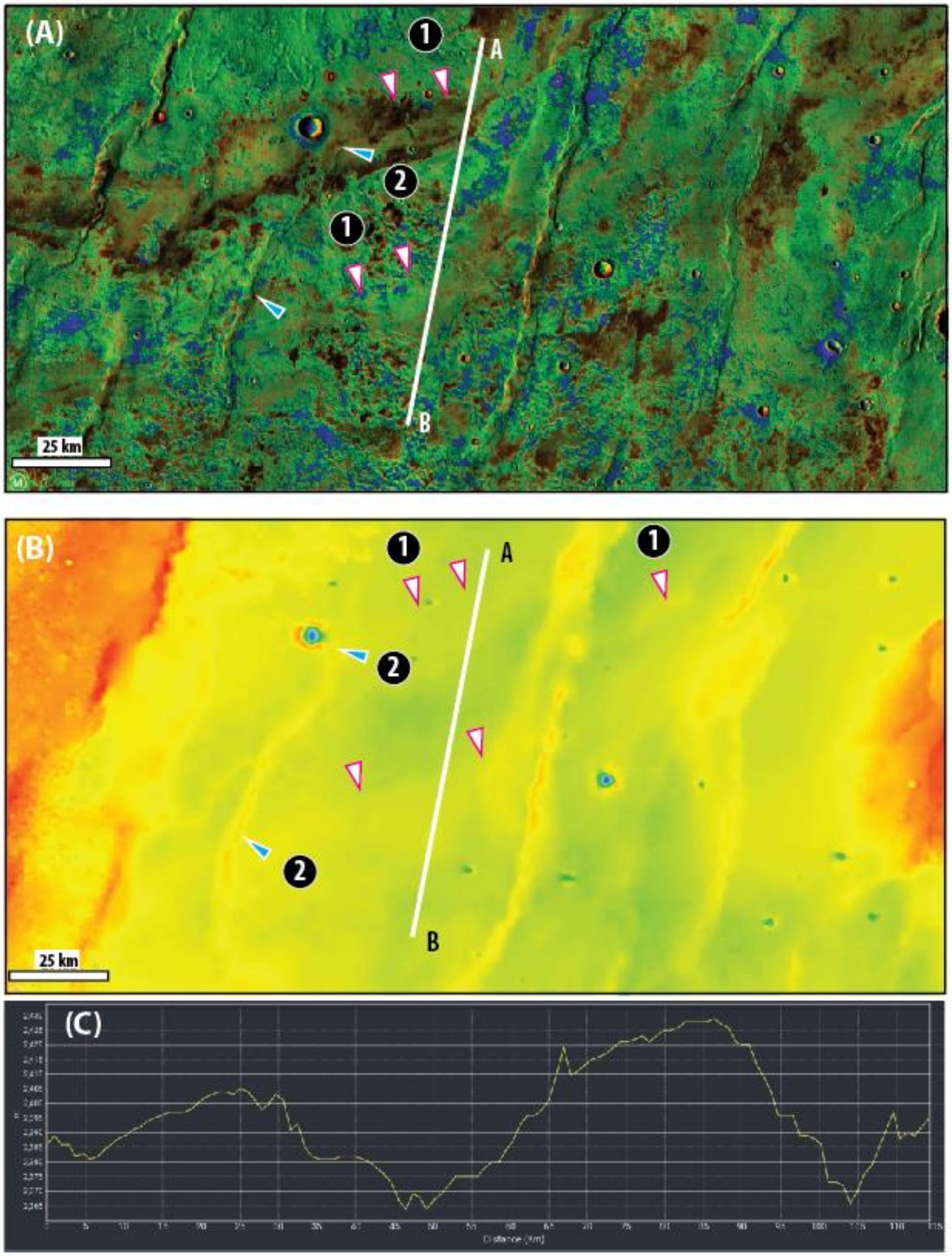

Figure 5

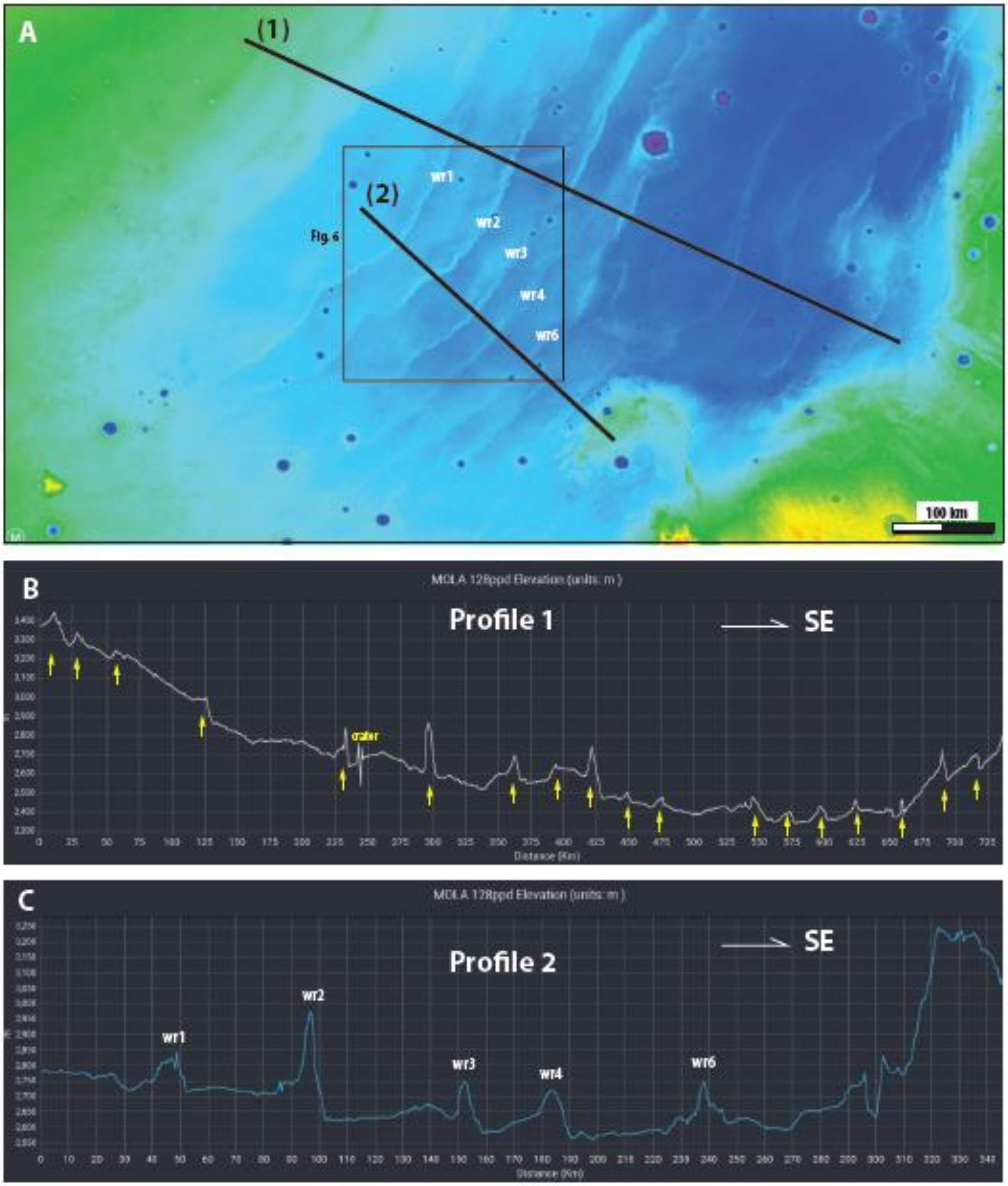

A
(1)
(2)
Fig. 6
wr1
wr2
wr3
wr4
wr6
100 km
B
MOLA 128ppd Elevation (units: m)
Profile 1
SE
crater
Distance (Km)
C
MOLA 128ppd Elevation (units: m)
Profile 2
SE
wr1
wr2
wr3
wr4
wr6
Distance (Km)

Figure 6

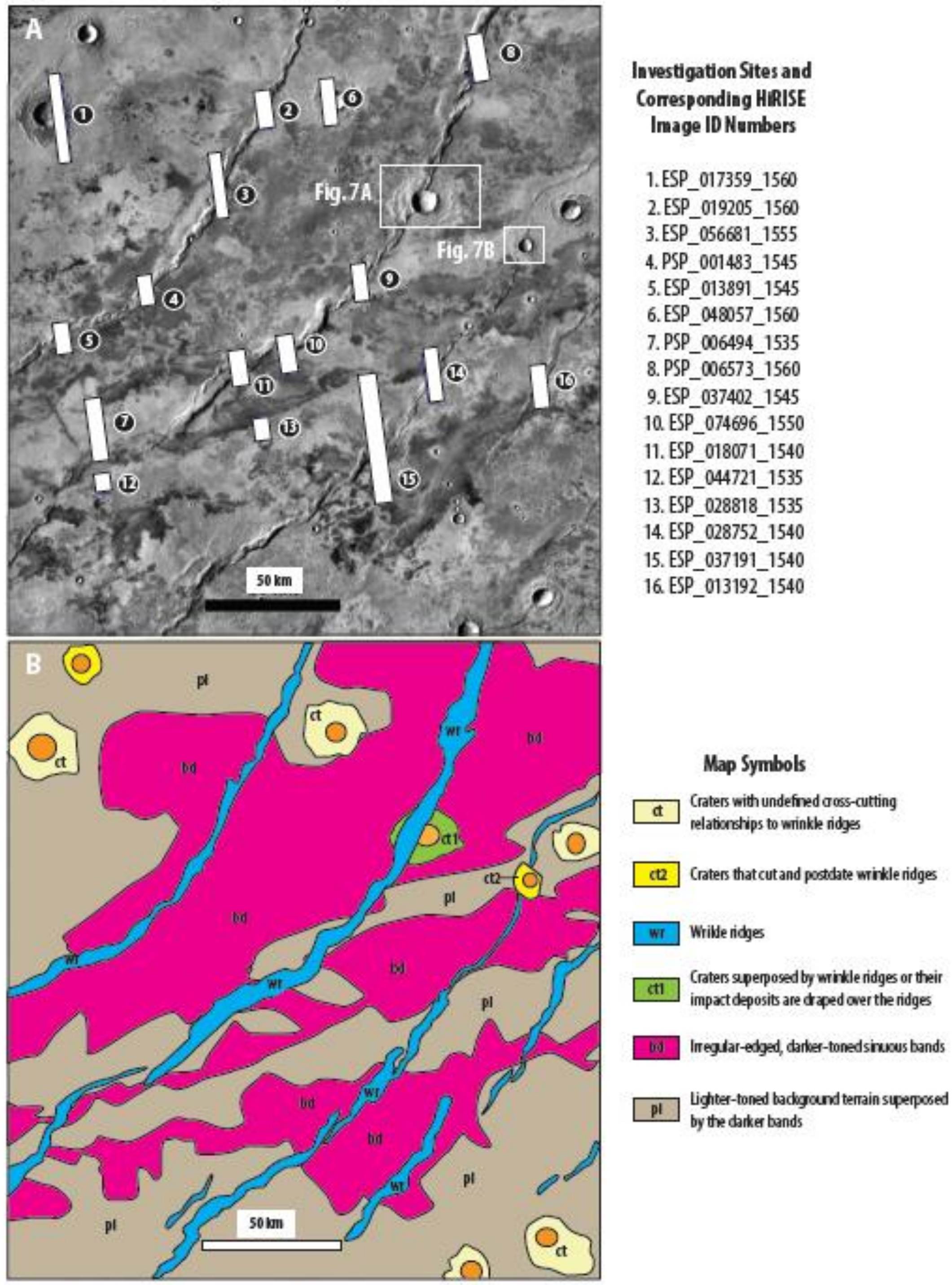
A
Fig. 7A
Fig. 7B
50 km
Investigation Sites and Corresponding HiRISE Image ID Numbers
1. ESP_017359_1560
2. ESP_019205_1560
3. ESP_056681_1555
4. PSP_001483_1545
5. ESP_013891_1545
6. ESP_048057_1560
7. PSP_006494_1535
8. PSP_006573_1560
9. ESP_037402_1545
10. ESP_074696_1550
11. ESP_018071_1540
12. ESP_044721_1535
13. ESP_028818_1535
14. ESP_028752_1540
15. ESP_037191_1540
16. ESP_013192_1540
B
pl
ct
bd
wr
ct1
ct2
50 km
Map Symbols
ct Craters with undefined cross-cutting relationships to wrinkle ridges
ct2 Craters that cut and postdate wrinkle ridges
wr Wrikle ridges
ct1 Craters superposed by wrinkle ridges or their impact deposits are draped over the ridges
bd Irregular-edged, darker-toned sinuous bands
pl Lighter-toned background terrain superposed by the darker bands

Figure 7

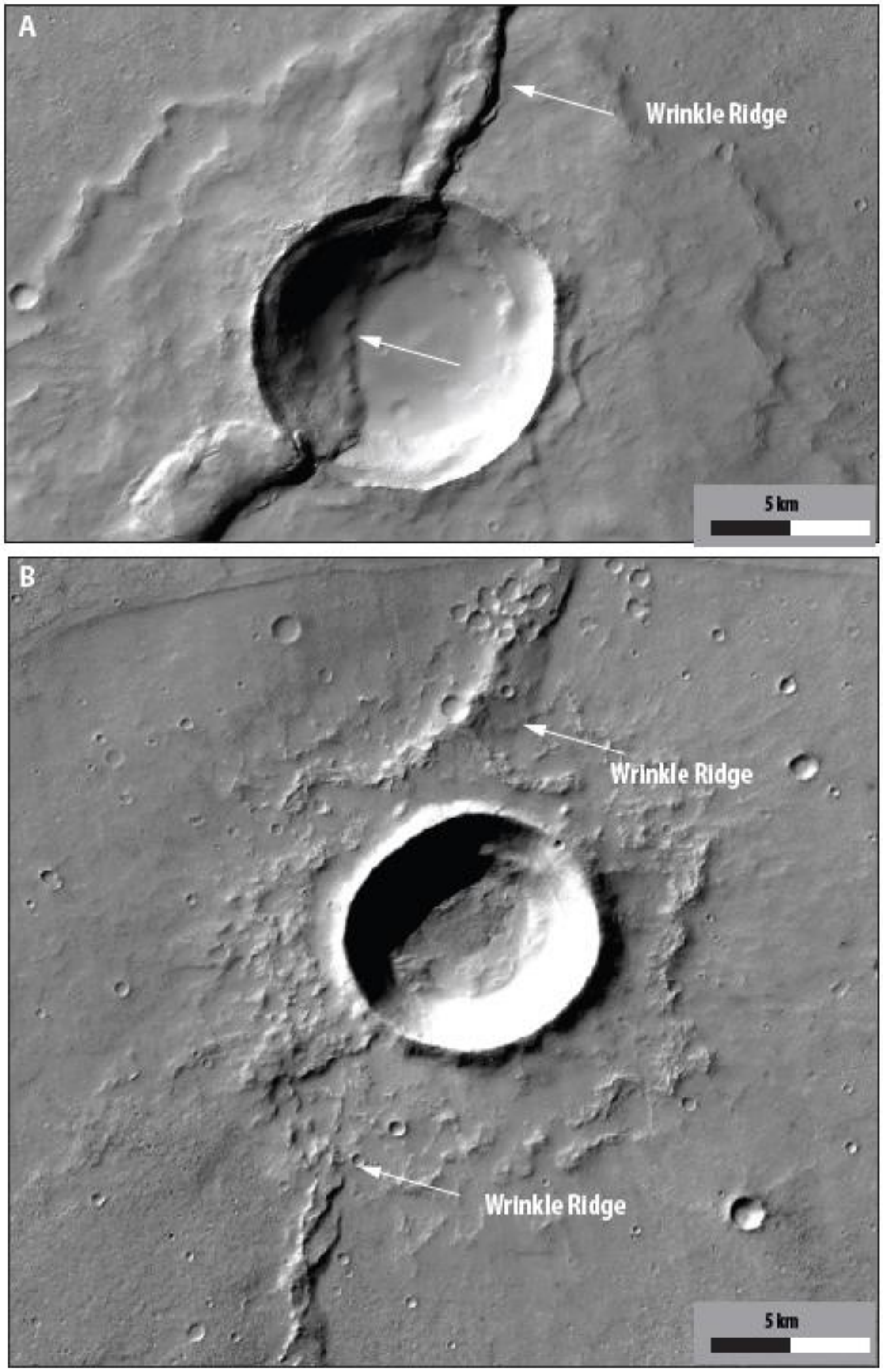

Figure 8

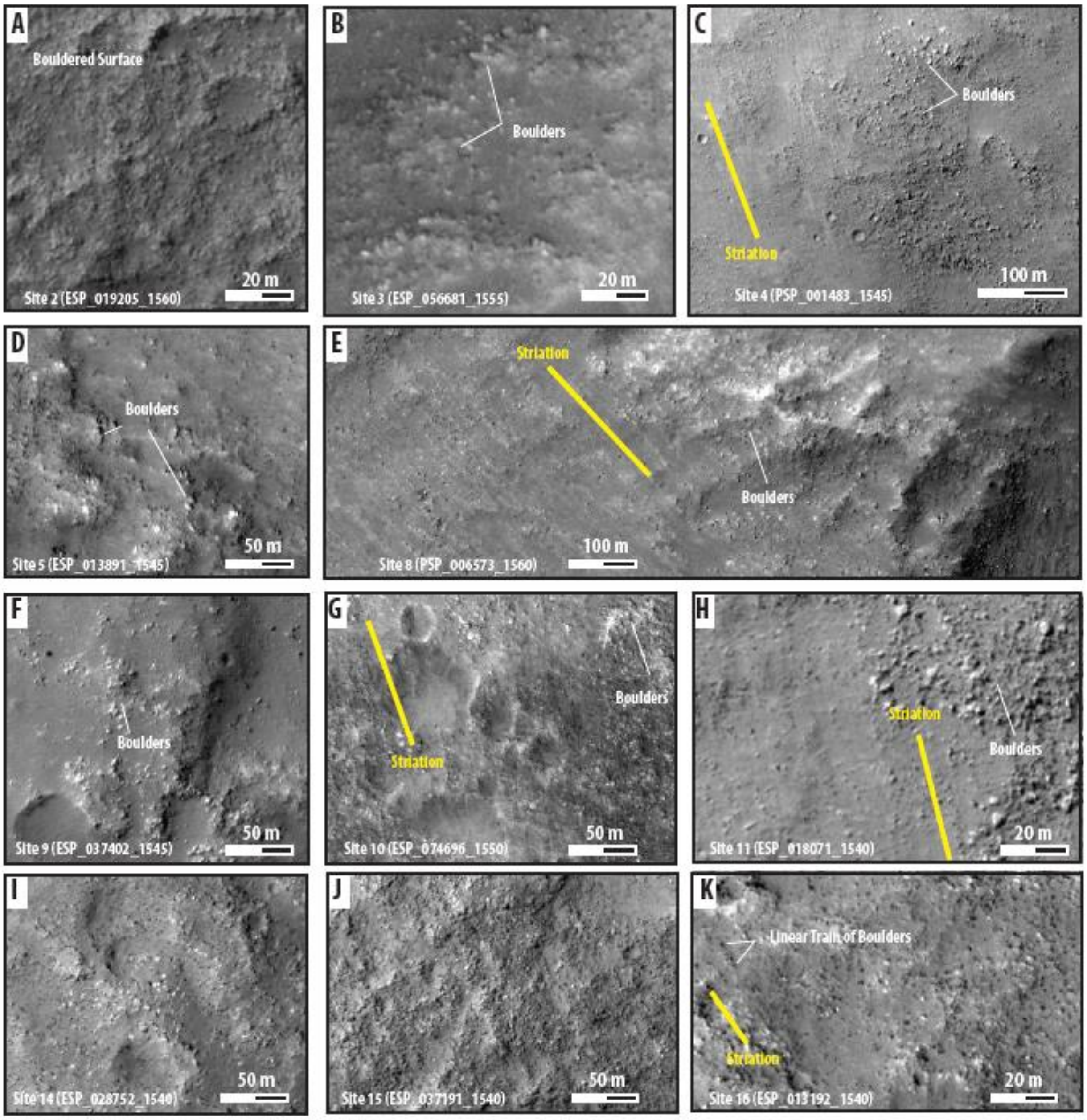

A
Bouldered Surface
20 m
Site 2 (ESP_019205_1560)
B
Boulders
20 m
Site 3 (ESP_056681_1555)
C
Boulders
Striation
100 m
Site 4 (PSP_001483_1545)
D
Boulders
50 m
Site 5 (ESP_013891_1545)
E
Striation
Boulders
100 m
Site 8 (PSP_006573_1560)
F
Boulders
50 m
Site 9 (ESP_037402_1545)
G
Boulders
Striation
50 m
Site 10 (ESP_074696_1550)
H
Striation
Boulders
20 m
Site 11 (ESP_018071_1540)
I
50 m
Site 14 (ESP_028752_1540)
J
50 m
Site 15 (ESP_037191_1540)
K
Linear Train of Boulders
Striation
20 m
Site 16 (ESP_013192_1540)

Figure 9

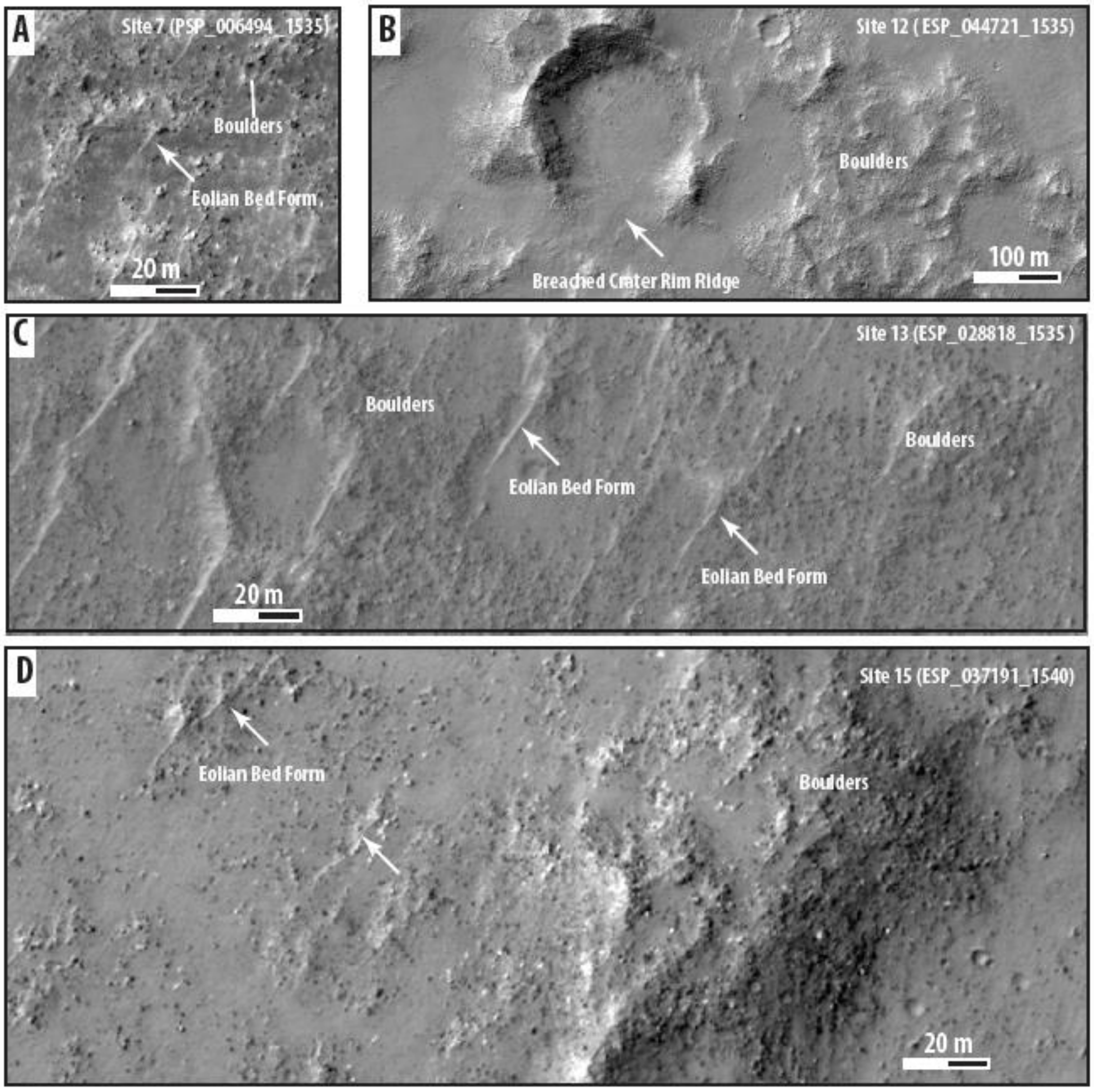
A
Site 7 (PSP_006494_1535)
Boulders
Eolian Bed Form
20 m
B
Site 12 (ESP_044721_1535)
Boulders
Breached Crater Rim Ridge
100 m
C
Site 13 (ESP_028818_1535)
Boulders
Boulders
Eolian Bed Form
Eolian Bed Form
20 m
D
Site 15 (ESP_037191_1540)
Eolian Bed Form
Boulders
20 m

Figure 10

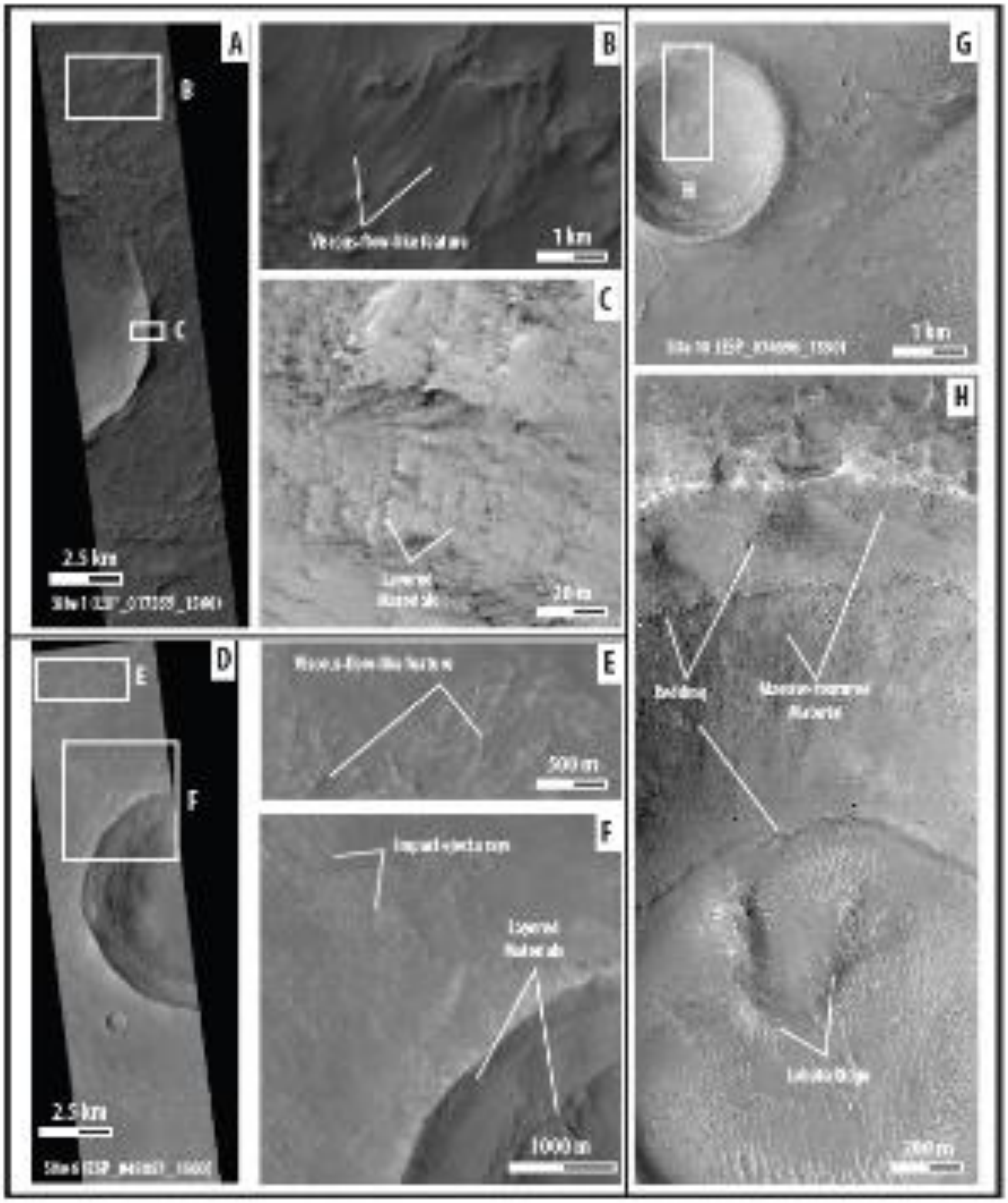
A
B
C
2.5 km
B
1 km
C
20 m
G
1 km
D
E
F
2.5 km
E
500 m
F
Impact ejecta rays
Layered Materials
1000 m
H
Bedding
Lobate Ridge
200 m

Figure 11

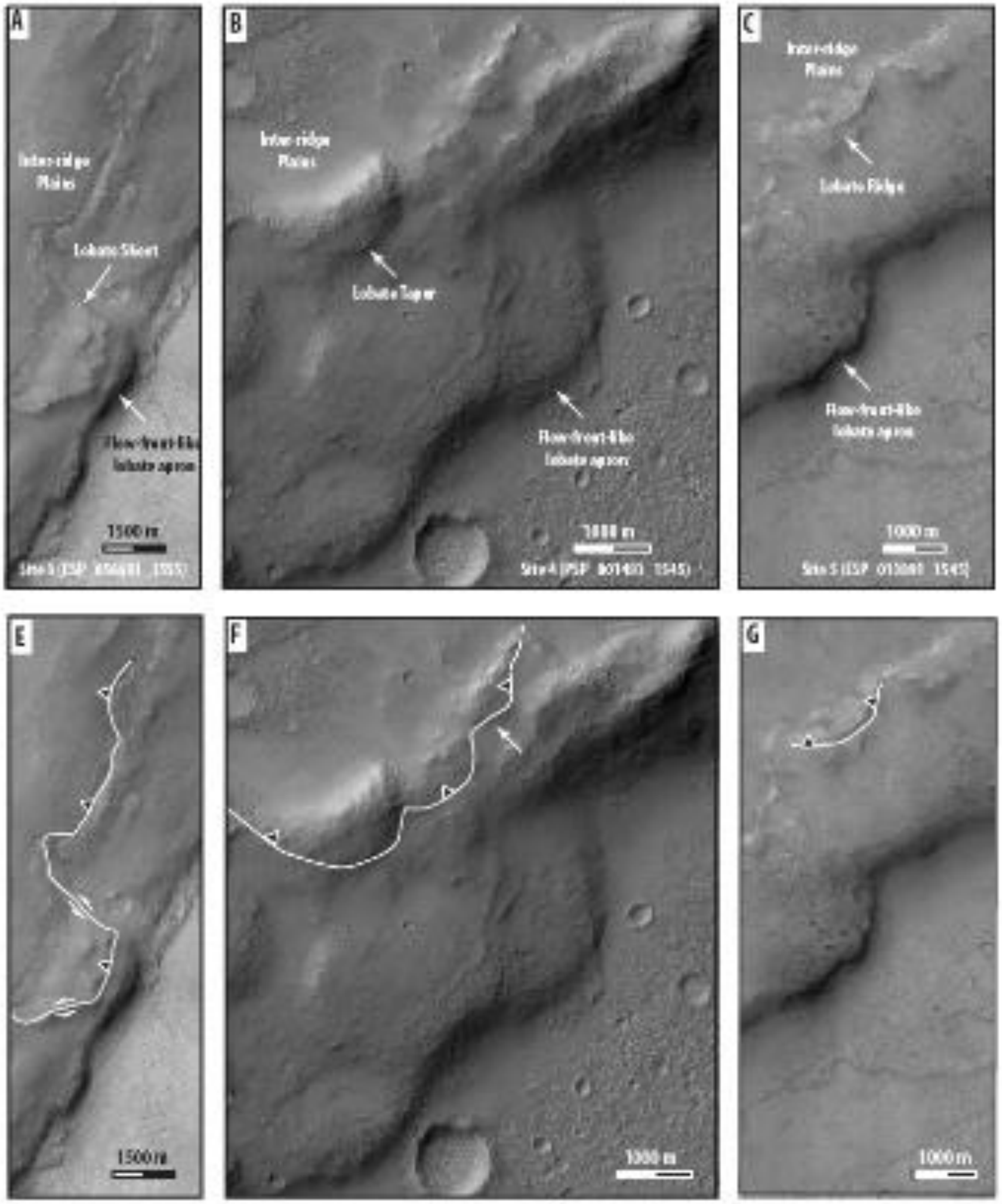
A
Inter-ridge Plains
Lobate Sheet
Flow-front-like lobate apron
1500 m
B
Inter-ridge Plains
Lobate Taper
Flow-front-like lobate apron
1000 m
C
Inter-ridge Plains
Lobate Ridge
Flow-front-like lobate apron
1000 m
E
1500 m
F
1000 m
G
1000 m

Figure 12

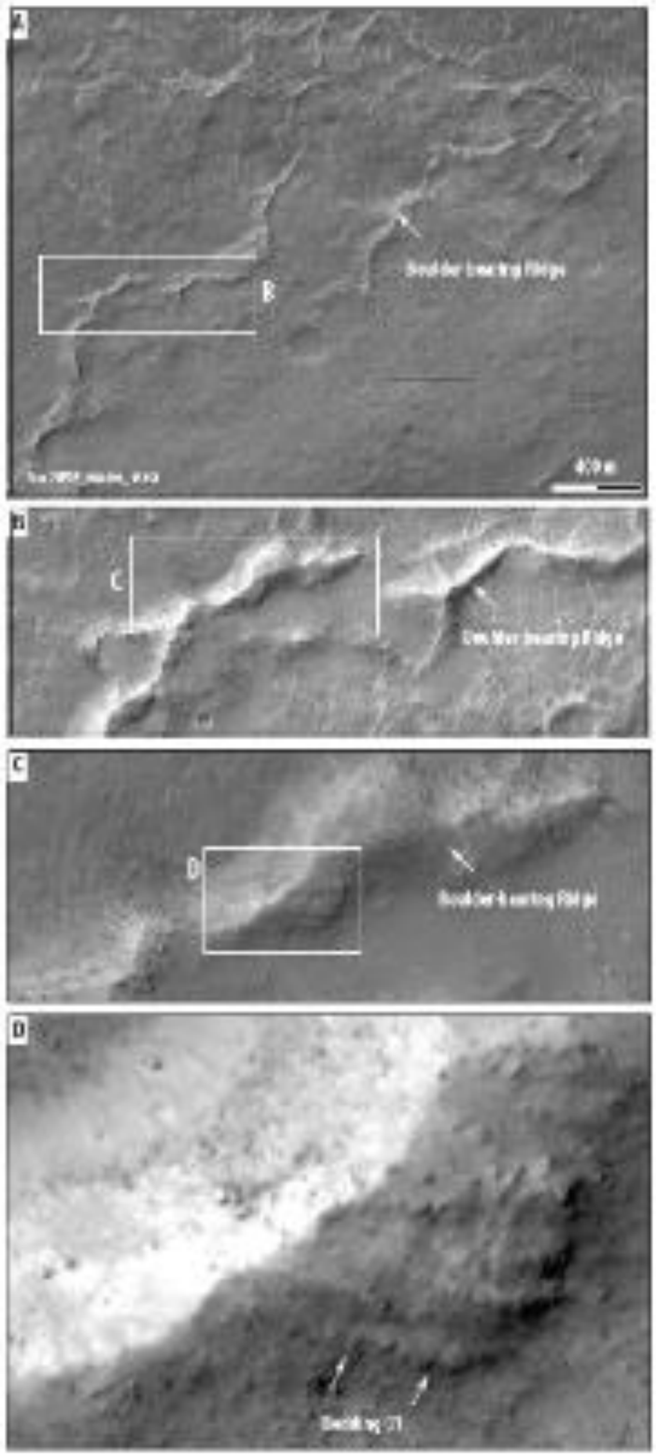

Figure 13

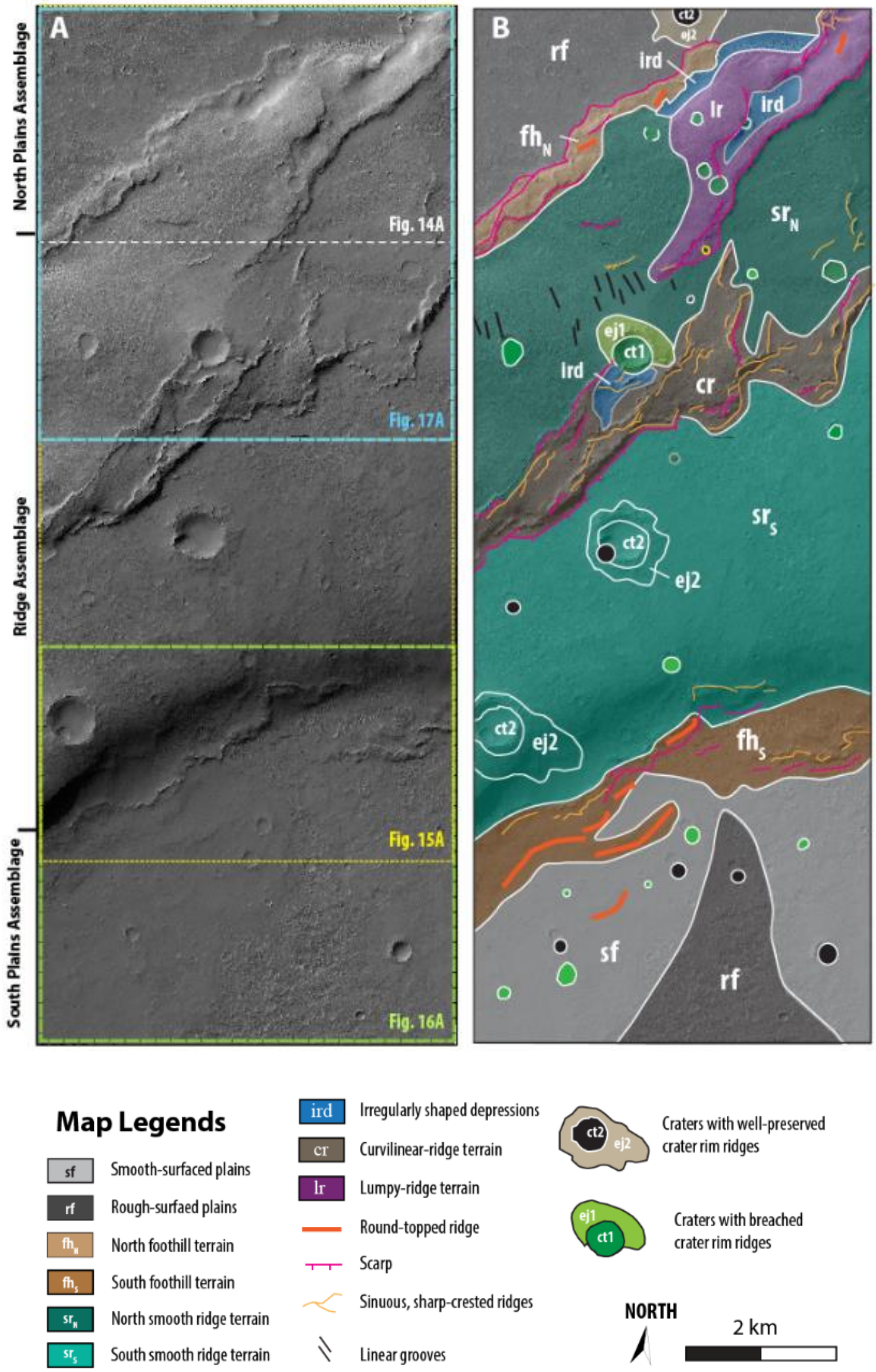

A
B
North Plains Assemblage
Ridge Assemblage
South Plains Assemblage
Fig. 14A
Fig. 17A
Fig. 15A
Fig. 16A
rf
ird
lr
ird
fhN
srN
ej1
ct1
ird
cr
ct2
ej2
srS
ct2
ej2
fhS
sf
rf
Map Legends
sf Smooth-surfaced plains
rf Rough-surfaed plains
fhN North foothill terrain
fhS South foothill terrain
srN North smooth ridge terrain
srS South smooth ridge terrain
ird Irregularly shaped depressions
cr Curvilinear-ridge terrain
lr Lumpy-ridge terrain
Round-topped ridge
Scarp
Sinuous, sharp-crested ridges
Linear grooves
ct2 ej2 Craters with well-preserved crater rim ridges
ej1 ct1 Craters with breached crater rim ridges
NORTH
2 km

Figure 14

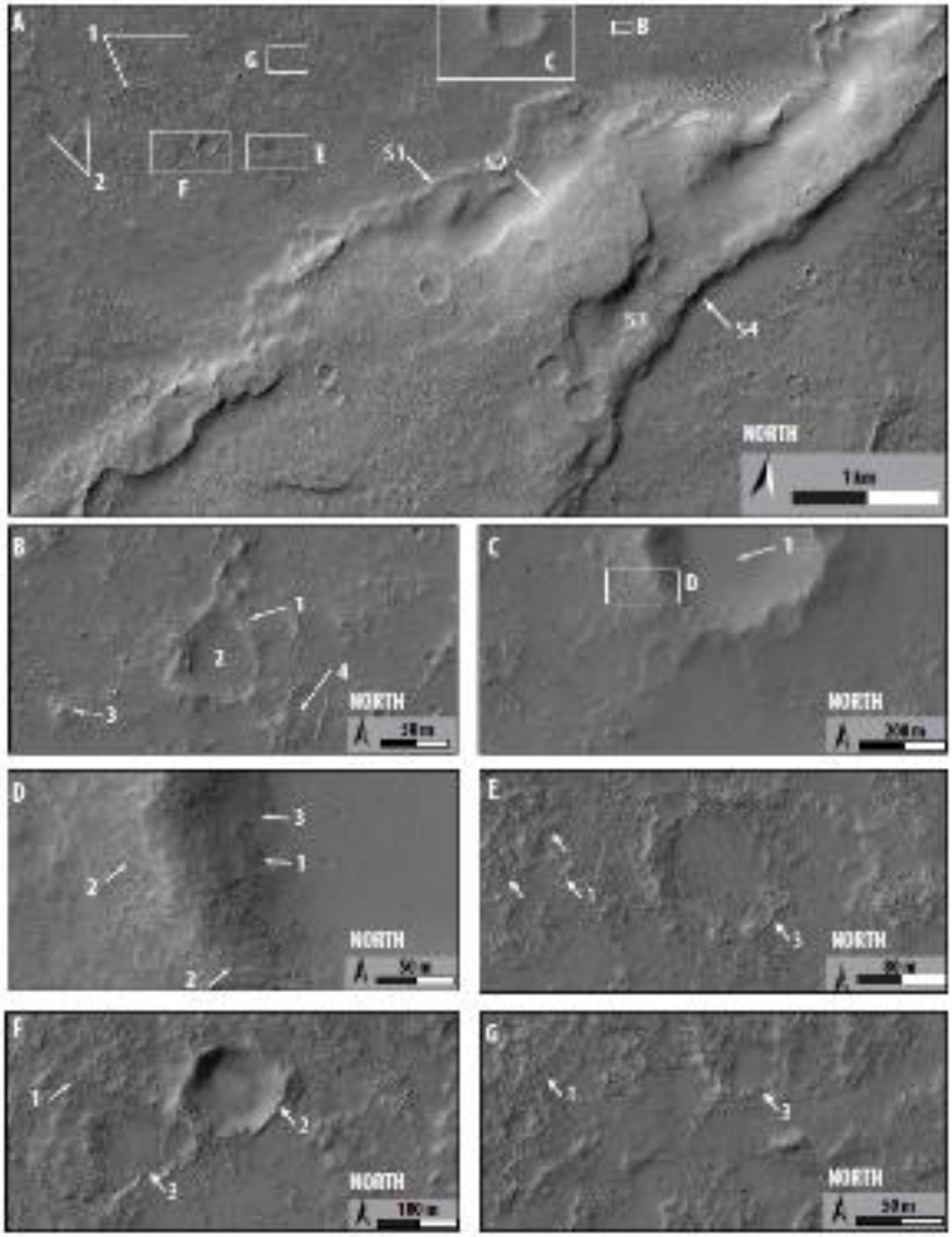
A
1
G
C
B
2
F
E
S1
S2
S3
S4
NORTH
1 km
B
1
2
4
3
NORTH
C
D
1
NORTH
D
3
1
2
2
NORTH
E
1
3
NORTH
F
1
2
3
NORTH
100 m
G
1
3
NORTH

Figure 15

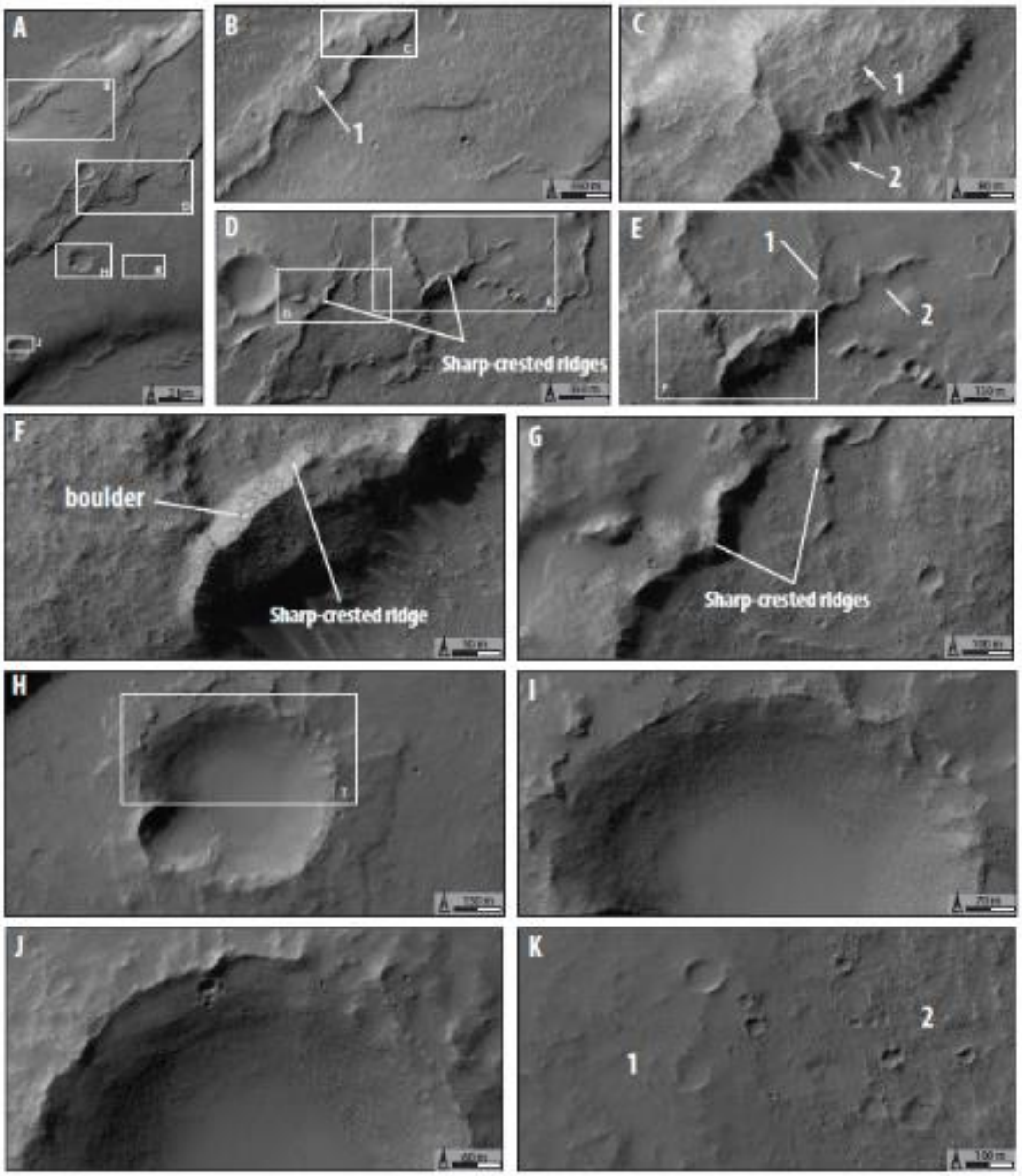
A
B
1
C
1
2
D
Sharp-crested ridges
E
1
2
F
boulder
Sharp-crested ridge
G
Sharp-crested ridges
H
I
J
K
1
2

Figure 16

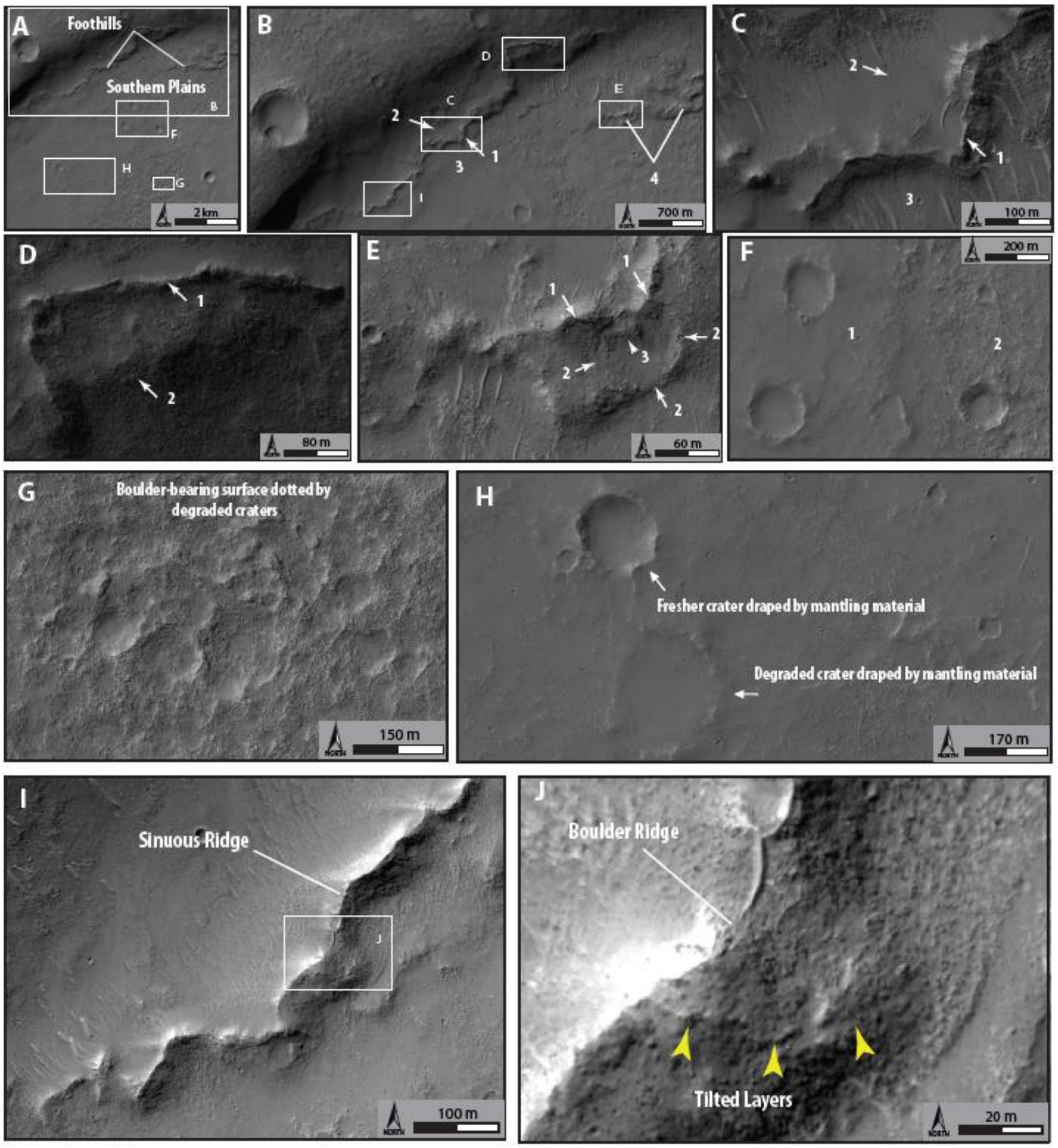
A
Foothills
Southern Plains
B
F
H
G
2 km
B
D
C
2
1
3
E
4
I
700 m
C
2
1
3
100 m
D
1
2
80 m
E
1
1
2
3
2
2
60 m
F
200 m
1
2
G
Boulder-bearing surface dotted by degraded craters
150 m
H
Fresher crater draped by mantling material
Degraded crater draped by mantling material
170 m
I
Sinuous Ridge
J
100 m
J
Boulder Ridge
Tilted Layers
20 m

Figure 17

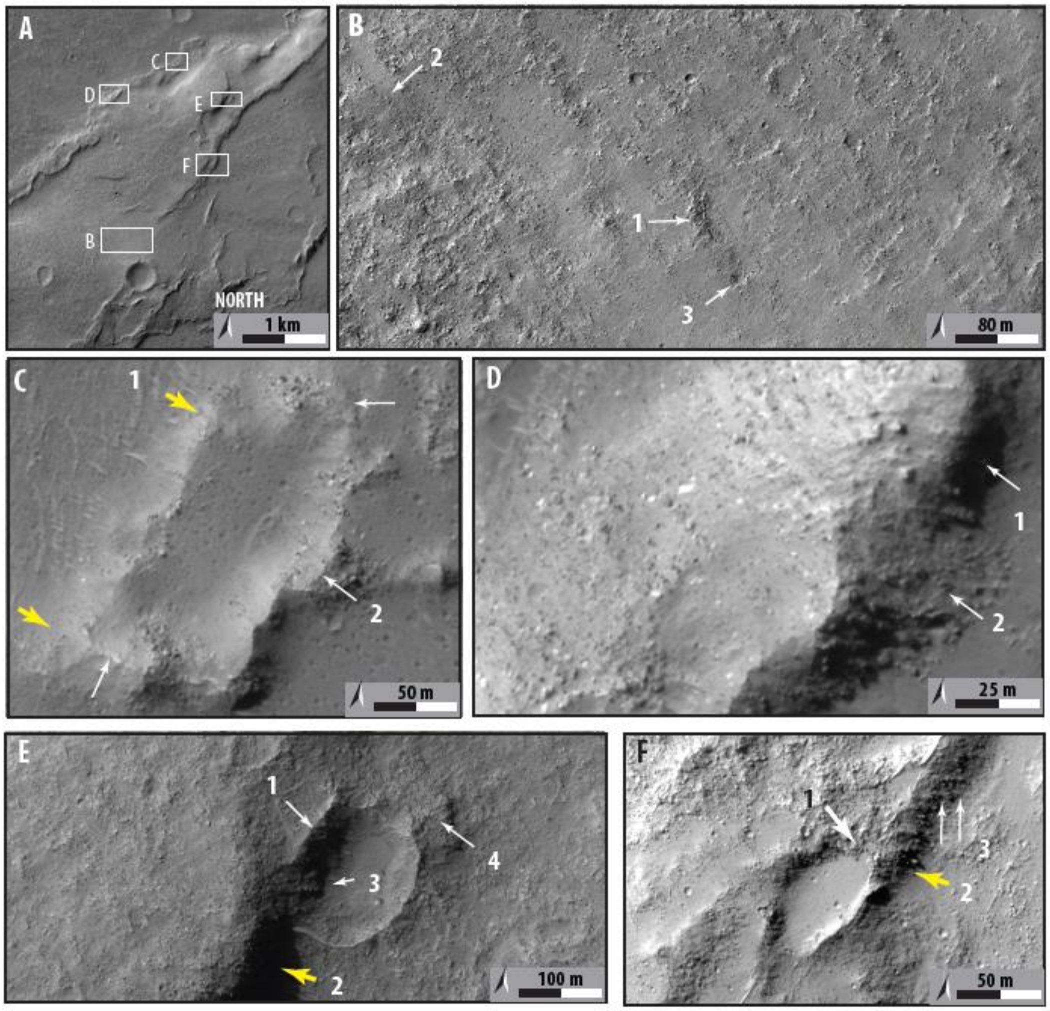

Figure 18

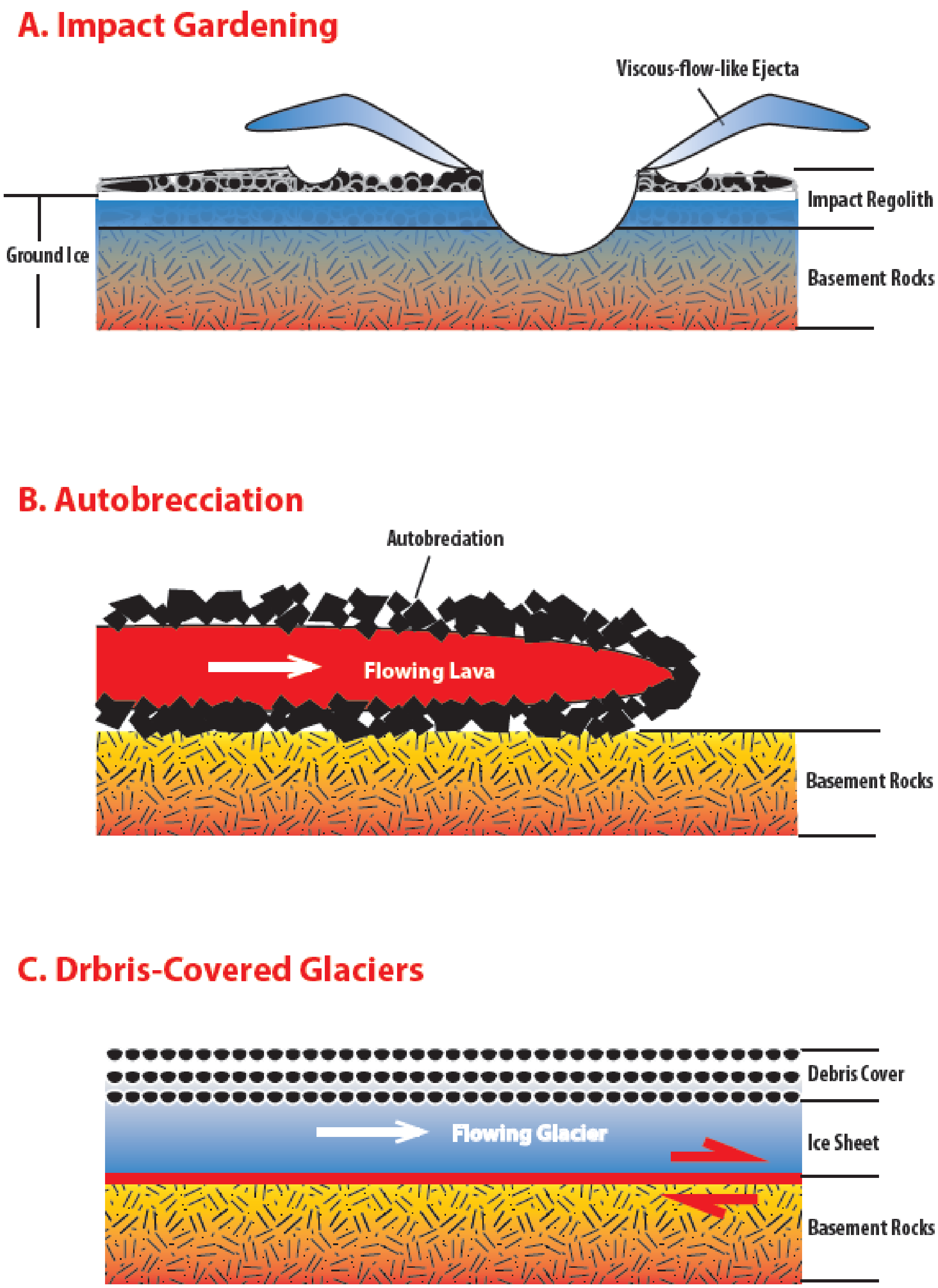
A. Impact Gardening
Viscous-flow-like Ejecta
Impact Regolith
Ground Ice
Basement Rocks
B. Autobrecciation
Autobreciation
Flowing Lava
Basement Rocks
C. Drbris-Covered Glaciers
Debris Cover
Flowing Glacier
Ice Sheet
Basement Rocks

Figure 19

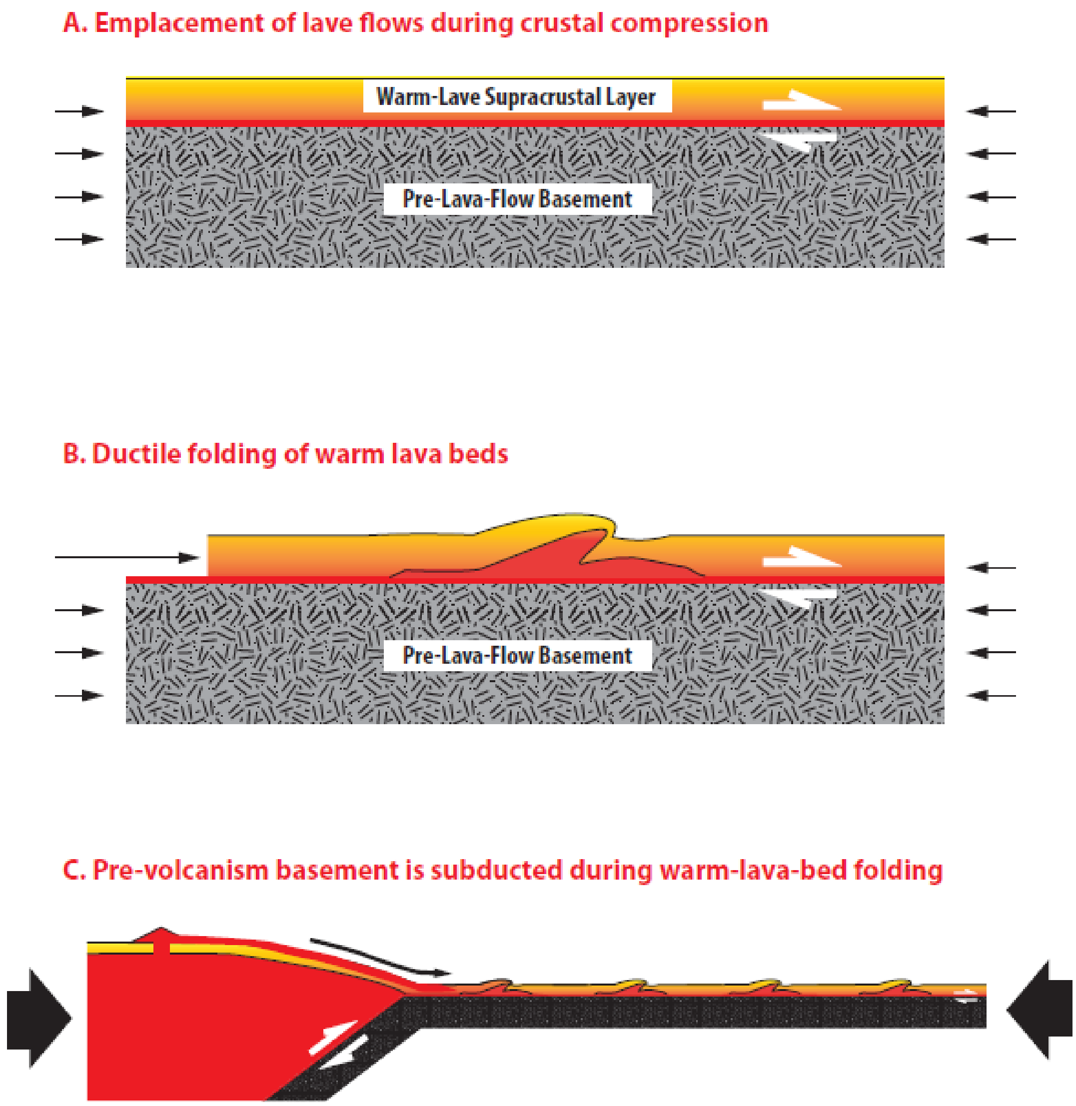
A. Emplacement of lave flows during crustal compression
Warm-Lave Supracrustal Layer
Pre-Lava-Flow Basement
B. Ductile folding of warm lava beds
Pre-Lava-Flow Basement
C. Pre-volcanism basement is subducted during warm-lava-bed folding

Figure 20

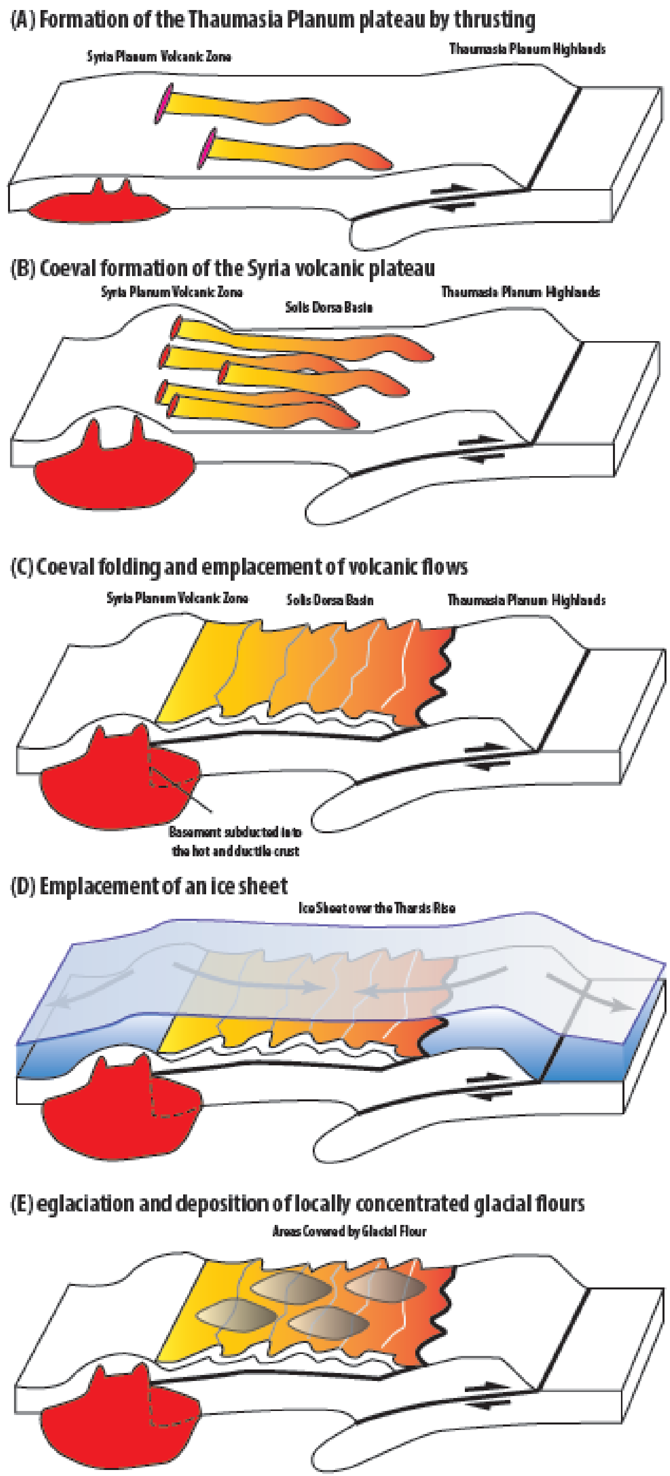

(A) Formation of the Thaumasia Planum plateau by thrusting
Syria Planum Volcanic Zone
Thaumasia Planum Highlands
(B) Coeval formation of the Syria volcanic plateau
Syria Planum Volcanic Zone
Solis Dorsa Basin
Thaumasia Planum Highlands
(C) Coeval folding and emplacement of volcanic flows
Syria Planum Volcanic Zone
Solis Dorsa Basin
Thaumasia Planum Highlands
Basement subducted into the hot and ductile crust
(D) Emplacement of an ice sheet
Ice Sheet over the Tharsis Rise
(E) eglaciation and deposition of locally concentrated glacial flours
Areas Covered by Glacial Flour